Simulations with the Marine Biogeochemistry Library (MARBL)

Matthew C. Long[1], Jefferson Keith Moore[2], Keith Lindsay[1], Michael N Levy[1], Scott C. Doney[3], Jessica Y. Luo[4], Kristen Marie Krumhardt[5], Robert T. Letscher[6], Maxwell Grover[5], and Zephyr T Sylvester[7]

[1]National Center for Atmospheric Research (UCAR)
[2]University of California, Irvine
[3]University of Virginia
[4]NOAA Geophysical Fluid Dynamics Laboratory
[5]National Center for Atmospheric Research
[6]University of Hampshire
[7]University of Colorado

November 21, 2022

Abstract

The Marine Biogeochemistry Library (MARBL) is a prognostic ocean biogeochemistry model that simulates marine ecosystem dynamics and the coupled cycles of carbon, nitrogen, phosphorus, iron, silicon, and oxygen. MARBL is a component of the Community Earth System Model (CESM); it supports flexible ecosystem configuration of multiple phytoplankton and zooplankton functional types; it is also portable, designed to interface with multiple ocean circulation models. Here, we present scientific documentation of MARBL, describe its configuration in CESM2 experiments included in the Coupled Model Intercomparison Project version 6 (CMIP6), and evaluate its performance against a number of observational datasets. The model simulates an air-sea CO_2 flux and many aspects of the carbon cycle in good agreement with observations. However, the simulated integrated uptake of anthropogenic CO_2 is weak, which we link to poor thermocline ventilation, a feature evident in simulated chlorofluorocarbon distributions. This also contributes to larger-than-observed oxygen minimum zones. Moreover, radiocarbon distributions show that the simulated circulation in the deep North Pacific is extremely sluggish, yielding extensive oxygen depletion and nutrient trapping at depth. Surface macronutrient biases are generally positive at low latitudes and negative at high latitudes. CESM2 simulates globally-integrated net primary production (NPP) of 48 Pg C yr^{-1} and particulate export flux at 100 m of 7.1 Pg C yr^{-1}. The impacts of climate change include an increase in globally-integrated NPP, but substantial declines in the North Atlantic. Particulate export is projected to decline globally, attributable to decreasing export efficiency associated with changes in phytoplankton community composition.

Simulations with the Marine Biogeochemistry Library (MARBL)

Matthew C. Long[1], J. Keith Moore[2], Keith Lindsay[1], Michael Levy[1], Scott C. Doney[3], Jessica Y. Luo[1,4], Kristen M. Krumhardt[1], Robert T. Letscher[5], Maxwell Grover[1], Zephyr T. Sylvester[6]

[1]Climate & Global Dynamics Laboratory, National Center for Atmospheric Research, Boulder, CO, USA
[2]Department of Earth System Science, University of California, Irvine, CA, USA
[3]Department of Environmental Sciences, University of Virginia, Charlottesville, VA, USA
[4]presently at Geophysical Fluid Dynamics Laboratory, National Oceanic and Atmospheric Administration, Princeton, NJ, USA
[5]University of New Hampshire, College of Engineering and Physical Sciences, Durham, NH, USA
[6]Environmental Studies Program, University of Colorado, Boulder, CO, USA

Key Points:

- MARBL is the ocean biogeochemistry component of the Community Earth System Model (CESM)
- MARBL is a flexible, plankton functional type model with a modular architecture supporting portability across ocean circulation models
- CESM2 CMIP6 solutions contain significant biogeochemical biases linked to underlying physics

Corresponding author: Matthew Long, `mclong@ucar.edu`

Abstract

The Marine Biogeochemistry Library (MARBL) is a prognostic ocean biogeochemistry model that simulates marine ecosystem dynamics and the coupled cycles of carbon, nitrogen, phosphorus, iron, silicon, and oxygen. MARBL is a component of the Community Earth System Model (CESM); it supports flexible ecosystem configuration of multiple phytoplankton and zooplankton functional types; it is also portable, designed to interface with multiple ocean circulation models. Here, we present scientific documentation of MARBL, describe its configuration in CESM2 experiments included in the Coupled Model Intercomparison Project version 6 (CMIP6), and evaluate its performance against a number of observational datasets. The model simulates an air-sea CO_2 flux and many aspects of the carbon cycle in good agreement with observations. However, the simulated integrated uptake of anthropogenic CO_2 is weak, which we link to poor thermocline ventilation, a feature evident in simulated chlorofluorocarbon distributions. This also contributes to larger-than-observed oxygen minimum zones. Moreover, radiocarbon distributions show that the simulated circulation in the deep North Pacific is extremely sluggish, yielding extensive oxygen depletion and nutrient trapping at depth. Surface macronutrient biases are generally positive at low latitudes and negative at high latitudes. CESM2 simulates globally-integrated net primary production (NPP) of 48 Pg C yr^{-1} and particulate export flux at 100 m of 7.1 Pg C yr^{-1}. The impacts of climate change include an increase in globally-integrated NPP, but substantial declines in the North Atlantic. Particulate export is projected to decline globally, attributable to decreasing export efficiency associated with changes in phytoplankton community composition.

Plain Language Summary

Numerical models of the ocean carbon cycle and biogeochemistry play a key role in understanding the fate of human carbon dioxide emissions and the magnitude of expected climate change over the next several decades to a century. Models are needed to quantify changes in the carbon reservoirs of the ocean and atmosphere and to explore interactions between climate change and carbon reservoirs that could amplify or damp future warming. This paper presents the Marine Biogeochemistry Library (MARBL), which is an ocean biogeochemistry model coupled to the Community Earth System Model (CESM). MARBL was designed to be compatible with multiple ocean models, a design motivated by an interest in building a diverse community of researchers around the development of MARBL. This paper presents a technical description of MARBL and an evaluation of the ocean biogeochemical simulation in CESM version 2. Overall, the model captures large-scale biogeochemical distributions, though several important biases are highlighted, including those dependent on the representation of circulation. MARBL provides a robust platform for researchers to address critical questions related to the impacts of climate variability and change on marine ecosystems.

1 Introduction

The ocean comprises the largest active carbon reservoir on Earth, storing approximately 38,000 Pg C of natural CO_2, nearly all of it as dissolved inorganic carbon (DIC). The ocean has also absorbed about 30% of anthropogenic CO_2 emissions (152 Pg through 2007) since the beginning of the industrial revolution (Sabine et al., 2004; Gruber et al., 2019)—and this sink will remain an important control on the airborne fraction of CO_2 emissions (Jones et al., 2013). Given this fundamental importance, Earth system models (ESMs) include ocean biogeochemistry models (OBMs) that seek to represent the ocean carbon cycle mechanistically, enabling future projections inclusive of carbon-climate feedbacks (Friedlingstein et al., 2006). As these models have matured, there has been increasing recognition of their relevance to questions beyond biogeochemistry, and in particular related to ocean ecosystems in the context of climate variability and change (Bopp

et al., 2013; Stock et al., 2011; Tommasi et al., 2017). This paper describes the Marine Biogeochemistry Library (MARBL), which is the ocean biogeochemistry component for the Community Earth System Model, version 2 (CESM2) (Danabasoglu et al., 2020). We document MARBL and evaluate the ocean biogeochemistry simulations in the fully-coupled CESM2 integrations submitted to the Coupled Model Intercomparison Project phase 6 (CMIP6) (Eyring et al., 2016).

In CESM2, MARBL was configured to invoke an updated version of what has previously been known as the Biogeochemistry Elemental Cycle (BEC) model (Moore et al., 2002, 2002a, 2004, 2013). MARBL is a modularized code base, however, consisting of a self-contained, independent Fortran library that interfaces with an ocean general circulation model (OGCM) through an explicit driver layer. This explicit design decision enables interoperability between MARBL and different physical models (see section 2.1). Moreover, MARBL has some flexibility with respect to the configuration of its ecosystem, supporting simulation of an arbitrary number of zooplankton and phytoplankton functional types (PFTs).

The BEC model has been under development for more than two decades, with initial roots in a one-dimensional configuration applied to represent the seasonal cycle of upper ocean primary production at the Joint Global Ocean Flux Study (JGOFS), Bermuda Atlantic Timeseries Study site (Doney et al., 1996). This formulation was extended by Moore et al. (2002) to include three phytoplankton functional types, multiple nutrient co-limitation (N, P, Si, Fe), nitrogen fixation, and calcification. At this point, the model was run in the mixed-layer on a global grid, but there was no lateral exchange and nutrient concentrations below the mixed layer were specified from an observationally-based climatology (Moore et al., 2002). The Moore et al. (2002) model was capable of reproducing the dominant patterns of primary production, nitrogen fixation, and export, including the observed high nitrate, low chlorophyll (HNLC) conditions in the Southern Ocean, Subarctic Northeast Pacific, and equatorial Pacific (Moore et al., 2002a). Moore et al. (2004) implemented the BEC model in a three-dimensional global OGCM for the first time, demonstrating skillful biogeochemical solutions under prognostic flow forced by meteorological fields from atmospheric reanalysis data. This implementation also enabled running the model in a "fully-coupled" context, in which atmospheric and ocean general circulation models exchange information via a flux coupler. A series of studies examined BEC solutions in the Community Climate System Model, version 3 (CCSM3) (Collins et al., 2006; Yeager et al., 2006). These include examinations of the effect of atmospheric nutrient deposition (Moore & Doney, 2007; Moore et al., 2006; Krishnamurthy et al., 2007, 2009, 2010; Han et al., 2008; Doney et al., 2007; Mahowald et al., 2011), climate-change impacts on ecosystems (Marinov et al., 2010), carbon-climate feedbacks (Thornton et al., 2009), the mechanisms driving carbon fluxes (Lovenduski et al., 2008; Wang et al., 2012; Doney et al., 2009) and the impacts of volcanic forcing on ocean biogeochemistry (Rothenberg et al., 2012). The Community Climate System Model evolved into the Community Earth System Model, and the BEC model was released to the community in this context. Moore et al. (2013) documented the marine ecosystem response to climate change in CESM1; Long et al. (2013) described the simulation of the present-day ocean carbon sink and Lindsay et al. (2014) examined the fully-coupled carbon cycle in CESM1. In addition to projections out to 2100, CESM1 was used to conduct Extended Representative Concentration Pathway (RCP) scenario integrations out to the year 2300 (Moore et al., 2018; Randerson et al., 2015). A version of CESM1 was used to conduct a large ensemble (CESM-LE) experiment (Kay et al., 2015), which included ocean biogeochemistry simulated by BEC. The CESM-LE enabled a series of studies that explicitly separated natural variability from anthropogenic forced trends in ocean biogeochemistry (Long et al., 2016; Lovenduski et al., 2015, 2016; McKinley et al., 2016; Krumhardt et al., 2017; Eddebbar et al., 2019). BEC has also been used in Decadal Prediction experiments with CESM1 (Yeager et al., 2012), and a handful of studies have examined

predictability of ocean biogeochemical dynamics in this framework (e.g., Krumhardt et al., 2020; Lovenduski et al., 2019; Yeager et al., 2018).

Our objectives in this paper are to document MARBL and specifically its configuration in the CESM2 integrations submitted to CMIP6. MARBL development has continued since the CMIP6 integrations were conducted, and there a handful of MARBL features that were not enabled in the CMIP runs. We refer to the CMIP6 configuration of MARBL, the default configuration in CESM2.1, as MARBL-CESM2.1 to explicitly note the associated model version and its configuration. That is, statements made about MARBL hold for all configurations of MARBL, as it was released in CESM2.1, and statements about MARBL-CESM2.1 hold for the default configuration in that release.

2 Model description

2.1 Flexible implementation

MARBL is a stand-alone Fortran library designed to be implemented in multiple OGCMs. The MARBL framework can be best understood by reference to the prognostic equation governing the evolution of an arbitrary passive tracer χ in an OGCM:

$$\frac{\partial \chi}{\partial t} + \nabla \cdot (\mathbf{u}\,\chi) - \nabla \cdot (K\,\nabla \chi) = J_\chi(\mathbf{x}), \tag{1}$$

where the terms on the left hand side (LHS) are the time-tendency, resolved three-dimensional advection by the simulated velocity field, $\mathbf{u}$, and diffusion determined by the diffusivity K. $J_\chi(\mathbf{x})$ is the sum of sources-minus-sinks for χ, computed as a function of the model state vector, $\mathbf{x}$; air-sea, benthic, or riverine fluxes provide boundary conditions. MARBL computes the source/sink terms and interfaces with an OGCM through an explicit driver layer, such that multiple OGCMs that have implemented the MARBL-driver can call the identical MARBL code. The OGCM computes the LHS of Eq. (1) and handles time-integration. MARBL has been implemented in the Parallel Ocean Program version 2 (POP2; the CESM2 ocean component) (Danabasoglu et al., 2012), the Model for Prediction Across Scales, Ocean (MPAS-O) (Ringler et al., 2013; Burrows et al., 2020), and the Modular Ocean Model, version 6 (MOM6) (Adcroft et al., 2019), which will be the ocean component in CESM3. MARBL is fully configurable at run-time, and is flexible enough to accommodate a variable number of plankton functional types and ecosystem configurations. MARBL is developed via an open-development process on GitHub, including continuous integration and testing, as well as tools supporting appropriate configuration in CESM integrations. The repository can be found at https://github.com/marbl-ecosys/MARBL.

2.2 Ocean biogeochemistry formulations

MARBL allows for easy addition of phytoplankton and zooplankton groups to the ecosystem. Both are treated as arrays, so to add a phytoplankton or zooplankton group simply requires specifying their parameter values in an input file. Key biogeochemical processes are built into MARBL, allowing the user to specify the biogeochemical functions associated with each phytoplankton group (i.e., calcifier, silicifier, capable of N fixation, etc.). This facilitates supporting multiple ecosystem configurations spanning a range in complexity. Here we focus on the implementation in CESM2 CMIP6 integrations, which preserved the ecosystem configuration in CESM1: MARBL-CESM2.1 includes one zooplankton group, three explicit phytoplankton functional groups (diatoms, diazotrophs, "small" pico/nano phytoplankton), and one implicit group (calcifiers). MARBL-CESM2.1 thus simulates 32 tracers, comprising 17 non-living constituents (dissolved inorganic carbon, alkalinity, nutrients, oxygen, and dissolved organic matter) and 15 tracers associated with living biomass. Carbonate chemistry is fully-explicit, and there are two par-

allel carbonate systems (e.g., with preindustrial and contemporary atmospheric CO_2), which enables cleanly computing anthropogenic CO_2 concentrations.

2.2.1 Phytoplankton growth

The source/sink term of the phytoplankton group (J_{P_i}) is

$$J_{P_i} = \mu_i P_i - G(P_i') - m_i T_f P_i' - A(P_i') \tag{2}$$

where the terms on the right-hand side represent growth, and sinks due to grazing (G), linear mortality (m_i) and aggregation (A). The loss terms are dependent on a P_i', which is the phytoplankton concentration in excess of a temperature- and depth-dependent threshold. The C-specific growth rate, μ_i, is parameterized as the product of the resource-unlimited growth rate (μ_{ref}) at a reference temperature (30°C), and temperature (T_f), nutrient limitation (V_i) and light availability (L_i) functions:

$$\mu_i = \mu_{ref} T_f V_i L_i. \tag{3}$$

The temperature dependence formulation,

$$T_f = 1.7^{\left(\frac{T - 30^\circ\mathrm{C}}{10^\circ\mathrm{C}}\right)}, \tag{4}$$

is based on results from Sherman et al. (2016).

Light-limitation is computed as a function of irradiance, I (W m^{-2}), using a modified form of the Geider et al. (1998, 1997) dynamic growth model,

$$L_i = 1 - \exp\left(\frac{-\alpha_i^{Chl}\theta_i^C I}{\mu_{ref} T_f V_i}\right), \tag{5}$$

where α_i^{Chl} (g C m^2 (g Chl W s)$^{-1}$) is the initial slope of the chlorophyll-a (Chl) specific photosynthesis-irradiance (PI) curve and θ_i^C is the chlorophyll to carbon ratio (g Chl:g C). This equation represents the growth rate as a function of the ratio between the supply of energy for photosynthesis in the form of instantaneous light harvesting capacity ($\alpha_i^{Chl} \cdot \theta_i^C \cdot I$), and the demand for growth in terms of the maximum photosynthetic rate constrained by temperature and nutrient limitation ($\mu_{ref} \cdot T_f \cdot V_i$). The chlorophyll to carbon ratio, θ_i^C, evolves prognostically in the model, thereby providing a representation of photoadaptation. The source/sink term for chlorophyll is

$$J_{Chl} = \rho_{Chl}\left(\frac{\mu_i}{r_{\mathrm{C:N}}\theta^C}\right) \tag{6}$$

where $r_{\mathrm{C:N}}$ is the carbon to nitrogen stoichiometry of phytoplankton (see below) and ρ_{Chl} is the dimensionless chlorophyll synthesis term (Geider et al., 1998), computed as

$$\rho_{Chl} = \theta_{max,i}^N \frac{\mu_i}{\alpha_i^{Chl}\theta_i^C I}. \tag{7}$$

Photosynthetically available radiation (I) is assumed to be 45% of incoming shortwave radiation (Doney et al., 1996). CESM simulates a subgrid-scale sea-ice thickness distribution and computes shortwave penetration independently for each ice thickness category, yielding multiple sub-columns with different light levels. MARBL computes all light-dependent terms on each sub-column independently, and then computes the grid-cell mean terms by taking an area-weighted average across sub-columns (Long et al., 2015). Since the photosynthesis equations are non-linear, this order of operations reduces numerical artifacts that arise where light fields are heterogeneous. Long et al. (2015) showed that this approach dramatically reduces biases in the simulation of high-latitude spring blooms relative to photosynthesis computed on grid-cell mean light.

Table 1. Model parameters.

Parameter	Value	Units	Description
μ_{ref}	5.0	d^{-1}	Maximum C-spec growth rate at Tref for small phytoplankton and diatoms
$\mu_{ref,\mathrm{diaz}}$	2.5	d^{-1}	Maximum C-spec growth rate at Tref for diazotrophs
Q_{10}	1.7	unitless	Q10 temperature coefficient
T_{ref}	30	°C	Reference temperature
$\theta^N_{max,\mathrm{sp}}$	2.5	mg Chl / mmol	Maximum θ^N (Chl / N) for small phytoplankton
$\theta^N_{max,\mathrm{diat}}$	4.0	mg Chl / mmol	Maximum θ^N (Chl / N) for diatoms
$\theta^N_{max,\mathrm{diaz}}$	2.5	mg Chl / mmol	Maximum θ^N (Chl / N) for diazotrophs
$\alpha^{Chl}_{\mathrm{sp}}$	0.39	mmol m^2/(mg Chl W day)	Chl-spec initial slope of P_I curve (GD98) for small phytoplankton
$\alpha^{Chl}_{\mathrm{diat}}$	0.28	mmol m^2/(mg Chl W day)	Chl-spec initial slope of P_I curve (GD98) for diatoms
$\alpha^{Chl}_{\mathrm{diaz}}$	0.39	mmol m^2/(mg Chl W day)	Chl-spec initial slope of P_I curve (GD98) for diazotrophs
$K^{\mathrm{Fe}}_{\mathrm{sp}}$	3.0e-05	mmol/m^3	Fe uptake half-sat constant for small phytoplankton
$K^{\mathrm{Fe}}_{\mathrm{diat}}$	7.0e-05	mmol/m^3	Fe uptake half-sat constant for diatoms
$K^{\mathrm{Fe}}_{\mathrm{diaz}}$	4.5e-05	mmol/m^3	Fe uptake half-sat constant for diazotrophs
$K^{\mathrm{NO_3}}_{\mathrm{sp}}$	0.25	mmol/m^3	NO3 uptake half-sat constant for small phytoplankton
$K^{\mathrm{NO_3}}_{\mathrm{diat}}$	0.5	mmol/m^3	NO3 uptake half-sat constant for diatoms
$K^{\mathrm{NO_3}}_{\mathrm{diaz}}$	2.0	mmol/m^3	NO3 uptake half-sat constant for diazotrophs
$K^{\mathrm{NH_4}}_{\mathrm{sp}}$	0.01	mmol/m^3	NH4 uptake half-sat constant for small phytoplankton
$K^{\mathrm{NH_4}}_{\mathrm{diat}}$	0.05	mmol/m^3	NH4 uptake half-sat constant for diatoms
$K^{\mathrm{NH_4}}_{\mathrm{diaz}}$	0.2	mmol/m^3	NH4 uptake half-sat constant for diazotrophs
$K^{\mathrm{PO_4}}_{\mathrm{sp}}$	0.01	mmol/m^3	PO4 uptake half-sat constant for small phytoplankton
$K^{\mathrm{PO_4}}_{\mathrm{diat}}$	0.05	mmol/m^3	PO4 uptake half-sat constant for diatoms
$K^{\mathrm{PO_4}}_{\mathrm{diaz}}$	0.015	mmol/m^3	PO4 uptake half-sat constant for diazotrophs
$K^{\mathrm{DOP}}_{\mathrm{sp}}$	0.3	mmol/m^3	DOP uptake half-sat constant for small phytoplankton
$K^{\mathrm{DOP}}_{\mathrm{diat}}$	0.5	mmol/m^3	DOP uptake half-sat constant for diatoms
$K^{\mathrm{DOP}}_{\mathrm{diaz}}$	0.075	mmol/m^3	DOP uptake half-sat constant for diazotrophs
$K^{\mathrm{SiO_3}}_{\mathrm{diat}}$	0.7	mmol/m^3	SiO3 uptake half-sat constant for diatoms
a^{min}_{sp}	0.01	d^{-1}	Minimum agg rate for small phytoplankton
a^{min}_{diat}	0.02	d^{-1}	Minimum agg rate for diatoms
a^{min}_{diaz}	0.01	d^{-1}	Minimum agg rate for diazotrophs
a^{max}_{sp}	0.5	d^{-1}	Maximum agg rate for small phytoplankton
a^{max}_{diat}	0.5	d^{-1}	Maximum agg rate for diatoms
a^{max}_{diaz}	0.5	d^{-1}	Maximum agg rate for diazotrophs
g^{max}_{sp}	3.3	d^{-1}	Maximum grazing rate at Tref for small phytoplankton
g^{max}_{diat}	3.15	d^{-1}	Maximum grazing rate at Tref for diatoms
g^{max}_{diaz}	3.3	d^{-1}	Maximum grazing rate at Tref for diazotrophs
K^P_i	1.2	mmol/m^3	Zooplankton grazing half saturation constant for all phytoplankton
γ_{sp}	0.3	unitless	Gross growth efficiency coefficient for grazing for small phytoplankton
γ_{diat}	0.25	unitless	Gross growth efficiency coefficient for grazing for diatoms
γ_{diaz}	0.3	unitless	Gross growth efficiency coefficient for grazing for diazotrophs
m_Z	0.1	d^{-1}	Zooplankton linear mortality rate at Tref
a_Z	0.4	d^{-1} / (mmol/m^3)	Zooplankton aggregation mortality rate at Tref

Phytoplankton nutrient requirements vary by taxa; diatoms (*diat*) require N, P, Si, and Fe, where as small phytoplankton (*sp*) and diazotrophs (*diaz*) do not assimilate Si and diazotrophs are not limited by N. Nutrient limitation is computed using Leibig's law of the minimum, such that

$$\begin{aligned} V_{diat} &= \min\left(V_{diat}^{\mathrm{N}}, V_{diat}^{\mathrm{P}}, V_{diat}^{\mathrm{Si}}, V_{diat}^{\mathrm{Fe}}\right), \\ V_{sp} &= \min\left(V_{sp}^{\mathrm{N}}, V_{sp}^{\mathrm{P}}, V_{sp}^{\mathrm{Fe}}\right), \text{ and} \\ V_{diaz} &= \min\left(V_{diaz}^{\mathrm{P}}, V_{diaz}^{\mathrm{Fe}}\right). \end{aligned} \tag{8}$$

Nutrient limitation is represented according to Michaelis-Menten kinetics, where

$$V_i^{\mathrm{Fe}} = \frac{\mathrm{Fe}}{\mathrm{Fe} + K_i^{\mathrm{Fe}}} \text{ and } V_i^{\mathrm{Si}} = \frac{\mathrm{SiO_3}}{\mathrm{SiO_3} + K_i^{\mathrm{SiO_3}}}. \tag{9}$$

However, phytoplankton can alternatively assimilate nitrate (NO_3) and ammonium (NH_4), following the substitutable model of O'Neill et al. (1989), such that

$$\begin{aligned} V_i^{\mathrm{NO_3}} &= \frac{\mathrm{NO_3}/K_i^{\mathrm{NO_3}}}{1 + \mathrm{NO_3}/K_i^{\mathrm{NO_3}} + \mathrm{NH_4}/K_i^{\mathrm{NH_4}}}; \\ V_i^{\mathrm{NH_4}} &= \frac{\mathrm{NH_4}/K_i^{\mathrm{NH_4}}}{1 + \mathrm{NO_3}/K_i^{\mathrm{NO_3}} + \mathrm{NH_4}/K_i^{\mathrm{NH_4}}}; \text{ and} \\ V_i^{N} &= V_i^{\mathrm{NO_3}} + V_i^{\mathrm{NH_4}}. \end{aligned} \tag{10}$$

All taxa are capable of assimilating both phosphate (PO_4) and semi-labile (see below) dissolved organic phosphate (DOP); a similar approach is used to compute limitation terms for these constituents.

Nutrient assimilation ratios are fixed for C:N according to Anderson and Sarmiento (1994) (117:16), but permitted to vary for P, Fe, and Si. P:C uptake for all PFTs is computed according to a modified version of the linear model of Galbraith and Martiny (2015). P:C uptake rates are linked to ambient phosphate concentrations, with P:C increasing linearly with increasing available phosphate, until a maximum P:C value is reached (Wang et al., 2019). The dynamic Fe:C ratios follow a similar formulation, with Fe:C ranging between specified minimum and maximum values as a function of ambient iron concentration (Moore et al., 2004). The Si:C uptake ratio for the diatoms is a function of both ambient iron and silicate concentrations, whereby low iron increases Si:C uptake and low silicate decreases the Si:C uptake ratio for new growth (Moore et al., 2004). As ambient nutrients concentrations change over time, phytoplankton nutrient assimilation ratios respond, leading to changes in the stoichiometry of phytoplankton biomass.

Loss of phytoplankton due to aggregation is parameterized as

$$A(P_i') = a_i P_i'^{1.75} \tag{11}$$

but constrained to fall between imposed minimum, $a_i^{min} \cdot P_i'$, and maximum, $a_i^{max} \cdot P_i'$, rates.

MARBL includes a representation of phytoplankton calcification as well as opal production by diatoms; these materials play an important role in mediating particulate organic carbon export (see below). Calcification in MARBL-CESM2.1 is treated implicitly as a varying fraction of the small phytoplankton NPP, similar to the approach in CESM1 (Moore et al., 2004). Baseline calcification is 7% of small phytoplankton NPP, but is decreased as nutrient limitation increases by multiplying calcification by the nutrient limitation term squared ($V_{sp}{}^2$). This decline in calcification under severe nutrient limitation aims to represent competition between calcifying coccolithophores and smaller picoplankton; calcification is thus reduced in the oligotrophic gyres where picoplankton have an advantage due to their larger cell surface-area-to-volume ratios (Moore et al.,

2002). Calcification is linearly reduced at temperatures below 4°C, reflecting the fact that coccolithophores are rare in polar waters (Iglesias-Rodríguez et al., 2002; Holligan et al., 2010). When small phytoplankton biomass exceeds 2.5 mmol C m^{-3}, calcification is scaled up to 40% of small phytoplankton production, providing a representation of enhanced calcification associated with blooms of the coccolithophore *Emiliania huxleyi*. Opal formation by diatoms is computed by multiplying diatom production by Si:C elemental ratio, which modified by Fe and Si ambient conditions, as described above.

2.2.2 Zooplankton

MARBL-CESM2.1 has one zooplankton class that grazes on phytoplankton according to a Holling Type II relationship

$$G(P_i') = g_i^{max} \cdot T_f \cdot \left(\frac{P_i'}{P_i' + K_i^P} \right) Z \tag{12}$$

The values of half-saturation constants, K_i^P, are identical for each phytoplankton taxa in MARBL-CESM2.1; the maximum grazing rates, g_i^{max}, vary, however, with diatoms experiencing the lowest grazing pressure. The temperature dependence of grazing, T_f, is the same as for phytoplankton growth and mortality. The source/sink equation for zooplankton is thus

$$J_Z = \gamma_{diat} G(P_{diat}') + \gamma_{sp} G(P_{sp}') + \gamma_{diaz} G(P_{diaz}') - m_Z T_f Z' - a_Z T_f Z'^{1.5} \tag{13}$$

where γ_i is a gross growth efficiency coefficient (Straile, 1997) and the last two terms on the right-hand side represent linear and aggregation mortality, respectively (see Table 1). Z' is the zooplankton concentration in excess of a depth-dependent threshold.

Zooplankton ingestion is partitioned into three fractions: converted to zooplankton biomass (γ_i), lost to egestion, and lost to respiration. The fraction of egestion losses (roughly 30% of ingestion, 45% for diatom prey) partitioned to sinking detritus varies by phytoplankton prey type, such that 10% and 38% of ingested diazotrophs and diatoms goes to POC, respectively. The fraction of the grazed small phytoplankton material routed to sinking particulate material varies as a function biomass, with reductions in the fraction exported at low biomass. The remainder of the egestion losses are partitioned to DOC (6% of ingestion for all phytoplankton types) and DIC (the remainder). Zooplankton respiration losses are assumed to be primarily a function of ingestion (40% for small phytoplankton and diazotrophs, and 30% for diatoms). The differential routing of zooplankton grazing is aimed at simulating various types of zooplankton (microzooplankton, mesozooplankton) within a single, "adaptive zooplankton" class.

Following Doney et al. (1996), zooplankton losses include linear and "quadratic" (here, "aggregation") loss terms. The linear losses represent a combination of metabolic and reproductive losses, as well as non-predatory mortality, while the aggregation losses approximately represent predation by unresolved higher trophic level predators (Fasham, 1995). The loss coefficients m_Z and a_Z are tuned to be consistent with overall mortality rates used in previous versions of the model (Doney et al., 1996; Moore et al., 2004, 2013). The routing of zooplankton losses to DIC, DOC, and POC are computed similarly for both linear and aggregation mortality losses; though, to simulate the effect of various zooplankton types, there are differential losses to POC based on phytoplankton prey type. 12% of zooplankton losses originating from grazing on small phytoplankton and diazotrophs, and 24% originating from grazing on diatoms, are routed to POC. Of the remainder, 6% is partitioned to DOC, which approximates the fraction of the semi-labile losses, and the remainder is routed to DIC.

Table 2. Remineralization length scales (in meters) for sinking particulate matter as a function of depth. The 100 m value is also used above that depth, and the 1000 m value is also used at deeper depths; for all values in between, the length scale is linearly interpolated from the values in the table.

depth (m)	POC	SiO_2	$CaCO_3$
100	100	650	500
250	360	2340	1800
500	470	3055	2350
1000	480	3120	2400

2.2.3 Detrital organic pools

There is no explicit sinking particulate organic matter (POM) tracer in MARBL; rather, sinking POM is simulated implicitly following Armstrong et al. (2002). In this formulation, sinking POM is redistributed in the water column as it is produced in each numerical timestep, with no time lag between surface production and deep remineralization. The redistribution follows the analytical solution to a first-order differential equation expressing POM flux as a function of a sinking velocity and remineralization rate, which together can be described by a remineralization length scale (Sarmiento & Gruber, 2006). Sinking POM is subject to ballasting by mineral dust, biogenic $CaCO_3$ and Si, which enhance the efficiency of export (Armstrong et al., 2002). Remineralization length-scales vary as a function of depth in MARBL, enabling a representation of the increasingly recalcitrant composition of sinking material at depth (Sarmiento & Gruber, 2006; Lima et al., 2014). In the CMIP6 integrations, the remineralization length scale was specified as 100 m for the upper 100 m, increasing by a factor of 4.8 by 1000 m (see Table 2 for the precise formulation). Remineralization length scales are also increased linearly in the presence of low oxygen (< 45 mmol m^{-3}). Remineralization rates have no dependence on temperature.

MARBL simulates 6 dissolved organic matter (DOM) pools, including semi-labile (SLDOM) and refractory dissolved organic (RDOM) carbon, nitrogen, and phosphorus (DOP) (Letscher & Moore, 2015; Letscher et al., 2015). MARBL does not include an explicit heterotrophic bacteria pool and thus does not capture the part of the "microbial loop" associated with assimilation of DOM by bacteria that are grazed by microzooplankton (Azam et al., 1983). The parameters controlling DOM cycling were optimized in an offline tracer-transport framework constrained by DOM observations (Letscher et al., 2015). Preferential remineralization of DOP leads to a DOM pool enriched in C and N relative to the composition of phytoplankton (Letscher & Moore, 2015). Both SLDOM and RDOM pools are produced from phytoplankton and zooplankton losses (mortality and aggregation; see above), as well as from grazing due to incomplete assimilation of grazed material. 6% of both the phytoplankton losses and grazing fluxes is routed to DOM and the fractional allocation of this material that flows to semi-labile and refractory pools is controlled via a fixed parameter. The refractory DOM pools also receive 6% of the POM remineralization flux. DOM remineralization has no explicit temperature dependence. DOM pools are remineralized at a rate determined by ambient light levels; remineralization rates for SLDOM are significantly higher in the dark (Letscher et al., 2015). The opposite is true for RDOM, where remineralization is enhanced in the presence of light due to photodegradation by ultraviolet light. SLDOM pools cycle with rates on the order of years; the RDOM pools have remineralization timescales of years at the surface increasing to many millenia at depth. Semi-labile DOP has an additional sink in the up-

per ocean associated with its use as a P source sustaining phytoplankton nutrient requirements when phosphate concentrations are low (Letscher et al., 2015).

2.2.4 Nitrogen cycle

MARBL simulates the marine nitrogen cycle with inputs from rivers, atmospheric deposition, and prognostic N fixation; losses of N include water column and sedimentary denitrification as well as ammonia emissions from the sea surface. Nitrogen fixation is simulated based on a fixed ratio of 1.25 between diazotroph N fixation and C fixation, which depends on adequate light and Fe availability. Diazotrophs are not limited by N, but do assimilate nitrate and ammonium when available—though given their much slower growth rates, they are at a competitive disadvantage relative to other taxa where in regions where N is not limiting.

Nitrification (the oxidation of ammonium to nitrite) is simulated as a first-order rate process dependent on the concentration of ammonium with a rate constant of 0.06 d^{-1}. The model does not explicitly simulate nitrite or N_2O: nitrification in the model thus represents both ammonium and nitrite oxidation and nitrate is the only product; there are no losses to N_2 via nitrification—therefore, nitrification does not result in losses of fixed N from the model ocean. Nitrification is light-inhibited and only occurs in MARBL where PAR is below 1 W m^{-2}. The subgrid-scale treatment of light (see above) is applied to the nitrification computation, such that nitrification is computed for each sub-column and the ultimate grid-cell mean is an area-weighted average across sub-columns. CESM simulates a diurnal light cycle, thus there is nitrification in the surface ocean at night.

Denitrification is the oxidation of organic matter via nitrate. Water column denitrification is simulated as a function of organic matter remineralization and local oxygen concentrations. Where oxygen declines below 10 mmol m^{-3}, the fraction of organic matter oxidation accounted for by denitrification is linearly increased until oxygen reaches 5 mmol m^{-3}, where denitrification is assumed to account for 100% of organic matter oxidation. MARBL also simulates sedimentary denitrification on the basis of an empirical relation depending on POC flux to the seafloor (Bohlen et al., 2012). Water column and sedimentary denitrification are reduced where nitrate concentrations approach zero. Denitrification does lead to fixed N loss from the model, to balance N fixation, but the N_2 product is not explicitly tracked. Oceanic emission of ammonia is simulated prognostically following Paulot et al. (2015).

2.2.5 Iron cycle

MARBL includes a representation of oceanic iron cycling that is an extension of the formulation described in Moore and Braucher (2008). Sources of dissolved iron to the ocean specified via forcing include dissolved iron inputs from sediments ($\sim$20 Gmol yr^{-1}), hydrothermal vents ($\sim$5.0 Gmol yr^{-1}), and rivers (0.37 Gmol yr^{-1}). The sedimentary iron source is applied using subgrid-scale bathymetry; this results in a vertical distribution of iron input in the water column, relative to simply applying the source at the model bottom. The sedimentary iron source is a temporally-static field; it is computed offline using a parameterization that depends on POC fluxes and bottom-current velocity simulated by CESM. The source of iron from oxic sediments is parameterized via a constant, low background value; this source is increased in regions of high bottom horizontal current speed (sediment re-suspension) according to the current velocity squared by up to a factor of 100. The source of iron from reducing sediments is linearly related to the sinking POC flux where the POC flux exceeds 3 g C m^{-2} yr^{-1}; below this threshold, the reducing sediment source is zero. This puts a source on the shelf, and along productive slope/margins, but has little source in the deep ocean, where almost all the remineralization is oxic right on the sediment surface. The two iron source types were combined

into one Fe input field for CESM2. Atmospheric deposition of soluble iron is computed prognostically as a function of dust and black carbon deposition provided by the atmospheric model. Dust also contributes sources of phosphate and silicate, following Krishnamurthy et al. (2010). The iron cycle includes a representation of scavenging (Moore & Braucher, 2008) and complexation by an explicit ligand tracer. The ligand tracer has sources due to remineralization and dissolved organic matter production.

2.2.6 Riverine forcing

Riverine nutrient (N, P, Si, Fe), dissolved inorganic carbon, alkalinity, and DOM fluxes are supplied to the CESM2 ocean model from a dataset, which includes nutrient loading estimates from GlobalNEWS (Mayorga et al., 2010) and the Integrated Model to Assess the Global Environment-Global Nutrient Model (IMAGE-GNM) (Beusen et al., 2016; Beusen et al., 2015). Nutrient inputs are provided for dissolved inorganic nitrogen (DIN), phosphorus (DIP), Si and Fe, as well as dissolved organic nitrogen and phosphorus. Carbon inputs are provided in inorganic and organic forms. Organic riverine inputs are partitioned into MARBL's corresponding semi-labile and refractory organic matter tracers; the fractions routed into the refractory tracers are 0.2, 0.1, and 0.025 for carbon, nitrogen, and phosphorus, respectively. Riverine DIC inputs are assumed to be comprised of 100% bicarbonate and thus alkalinity fluxes are equal to DIC fluxes. Particulate constituents are assumed to be removed in estuaries and therefore are not included in the riverine forcing supplied to the model. GlobalNEWS does not include dissolved iron inputs to the oceans; for the riverine Fe source we assumed a constant river concentration of 10 nM in a climatological runoff for the current era. Riverine nutrients and carbon fluxes are held constant using the GlobalNEWS data with the exception of DIN and DIP fluxes, which are taken from IMAGE-GNM and vary from 1900 through 2000; outside of this period, the fluxes are held constant using the closest temporal value.

In CESM2, the handling of riverine freshwater inputs was changed relative to previous versions of the model. In particular, rather than spreading riverine freshwater inputs out over a relatively large prescribed region of the ocean surface, CESM2 routes riverine freshwater input into the ocean column closest to location of the riverine input. A box-model framework is used to parameterize vertical estuary exchange flow and associated mixing of river and seawater prior to applying the input to the ocean column (Sun et al., 2017). This estuary box-model framework is also used in CESM2 to distribute riverine biogeochemical inputs, ensuring consistent treatment of freshwater and biogeochemical riverine inputs, and also avoiding the unrealistic spreading of inputs over a large region of the surface ocean.

2.2.7 Benthic processes

Riverine nutrient and carbon fluxes in CESM2 introduce material into the coupled system without a direct compensating sink from the land model. To avoid drift in ocean nutrient inventories and spurious accumulation of carbon in the atmosphere, ocean losses must balance riverine inputs. The marine nitrogen cycle in MARBL is open, capable of achieving a dynamic equilibrium as nitrogen fixation and denitrification come into balance with the other supply terms. Carbon, phosphorus, and silica inputs, by contrast, are balanced with the process of burial at the seafloor.

MARBL computes burial and denitrification losses of material at the seafloor according to empirical relationships. Particulate organic carbon burial is computed using a relationship between burial efficiency and POC flux from Dunne et al. (2007), with an imposed maximum burial efficiency of 80%. Burial of SiO_2 at the seafloor is based on observations in Ragueneau et al. (2000). In MARBL, 4% of Si incident on the seafloor is buried, except where the incident flux of Si to the seafloor exceeds 2 mmol m^{-2} d^{-1}; then, 20% of Si is buried. As described above, sedimentary denitrification depends on

the incident POC flux and is computed based on an empirical relationship from Bohlen et al. (2012). Burial of $CaCO_3$ on the ocean floor occurs where $\Omega > \Omega_{crit}$ in the model's bottom layer; where $\Omega < \Omega_{crit}$, all $CaCO_3$ reaching the model's bottom layer is dissolved. All $CaCO_3$ is assumed to be calcite, thus ignoring the distinction between the mineral forms calcite and aragonite, which may be important in modulating dissolution depths (Gangstø et al., 2008).

In order to achieve balanced global ocean tracer inventories, we impose global coefficients that scale burial of carbon, phosphorus, and silicon linearly following application of the initial empirical relationships. The burial scaling factor for particulate organic nitrogen is the same as for particulate organic carbon. These coefficients enable enforcing a match between globally-integrated burial and global riverine inputs, thus enforcing equilibrium in the preindustrial climate. The global burial coefficients were tuned online in a spin-up configuration (see below), adjusting the coefficient to force burial to match inputs on a 10-year timescale. To enable this, we compute an exponentially-weighted moving average of each term online in the model, thus filtering out temporal variability below the 10-year timescale, and adjusting the coefficients at each time step. Ω_{crit} was also tuned in the spin-up runs, to ensure a balanced alkalinity inventory.

2.2.8 Dissolved oxygen

During the ocean-tracer spin-up of the CESM2 model, we found that ventilation of the deep North Pacific was very sluggish in the coupled model, leading to severe oxygen depletion over a large portion of the interior water column. The problem is evidenced by simulated natural radiocarbon age in the deep North Pacific being twice that of observations (see Results). We were not able to alleviate the oxygen depletion by compensating for the circulation bias via tuning of MARBL parameters and it was too late in the CMIP6-driven development cycle to explore changes in the coupled model configuration to improve the ventilation. While ventilation biases are common in coarse resolution OGCMs, the North Pacific oxygen depletion in the spin up was so intense and widespread that we were concerned about large-scale denitrification leading to extensive loss of fixed nitrogen, which would perturb other aspects of the ocean biogeochemical simulation. Therefore, we were forced to address the problem via ad hoc means: we implemented a scale factor to reduce oxygen consumption in the North Pacific; oxygen consumption is multiplied by this scale factor, which was set to 0.3 in the deep Pacific (below 1500 m and north of 20°S) and 1.0 elsewhere; the scale factor changes linearly from 1.0 at 40°S to 0.3 at 20°S and similarly between 750 m and 1500 m depth. This ad hoc scaling of oxygen consumption breaks stoichiometric relationships between oxygen and other biogeochemical tracers, invalidating assumptions commonly made in the analysis of biogeochemical simulations (e.g., computing preformed nutrients). In order to avoid confusion from potential users of CESM2 CMIP6 output, we opted to withhold publication of oxygen-related fields from CESM2 CMIP6 experiments.

2.2.9 MARBL features not enabled in CMIP6

The CESM2-CMIP6 integrations include calcification simulated by the implicit calcification treatment described above. Recent developments have parameterized a prognostic phytoplankton calcifier in MARBL that is modeled on coccolithophore physiology (Krumhardt et al., 2019). The ratio of calcification to photosynthesis ($r_{CaCO_3:C}$) by the coccolithophore functional type is responsive to environmental conditions, where $r_{CaCO_3:C}$ is a function of temperature, nutrients, and CO_2. This enables a calcification response to ocean acidification, among other environmental changes (for further details see Krumhardt et al., 2019).

MARBL includes a representation of carbon isotopes, which follows on the implementation in POP by Jahn et al. (2015). The carbon isotope tracers in MARBL were

not enabled for the CESM2 CMIP6 integrations. An abiotic radiocarbon tracer implemented in POP was enabled for these runs, however (see below).

As mentioned above, the number and definition of plankton functional types in MARBL is flexible and can be configured at runtime via an input file. Ecosystem models with additional resolved plankton groups may be useful for coupling with models of higher trophic levels, providing a framework for understanding climate-driven variations in potential fisheries yield, for instance. The Size-based Plankton Ecological Traits (SPECTRA) version of MARBL employs allometric, i.e., size-based, scaling for various aspects of organismal physiology such as metabolic rates, resource acquisition, mortality, and predator-prey interactions, while maintaining important "trait-based" functions that are important for elemental cycles (e.g., opal production by diatom groups). The resulting MARBL-SPECTRA configuration has nine phytoplankton and six zooplankton PFTs representing various planktonic taxa within the 0.5 μm to 20mm size range, allowing explicit simulation of food resources for higher trophic levels.

2.2.10 Ancillary tracers

The simulated circulation of an ocean model plays a critical role in the ability of the ocean model to skillfully simulate biogeochemical tracers (Doney et al., 2004). In CESM2 experiments for CMIP6, the ocean model was run with several ocean diagnostic tracers: abiotic radiocarbon, chlorofluorocarbons (CFCs), and sulfur hexafluoride (SF_6). These tracers provide information about the ocean model's circulation that is relevant to the simulation of biogeochemical tracers. In particular, the natural component of abiotic radiocarbon provides information about the ocean model's circulation on multi-centennial and longer timescales, due to its 5730-year half-life. This information is complemented on decadal time-scales by the bomb-spike component of abiotic radiocarbon and the CFC and SF_6 tracers. While these diagnostic tracers are not included in the MARBL library, we analyze some aspects of their simulated values to put the analysis of the MARBL tracers in the appropriate context of the simulated flow. The implementation of these diagnostic tracers in CESM2 follows the protocols described in Orr et al. (2017). The abiotic radiocarbon implementation is largely based on the implementation described in Jahn et al. (2015).

Following Orr et al. (2017), the abiotic radiocarbon tracer is implemented as two abiotic tracers, $\mathrm{DIC}^{\mathrm{abio}}$ and $^{14}\mathrm{DIC}^{\mathrm{abio}}$. Because these tracers are abiotic, they are not directly comparable to observations individually. We instead compare to $\Delta^{14}\mathrm{C}$, the isotopic fractional abundance of $^{14}\mathrm{C}$ compared to $^{12}\mathrm{C}$, corrected for biological fractionation and normalized by dividing $^{14}\mathrm{C}/^{12}\mathrm{C}$ by $^{14}r_{\mathrm{std}}$, which is $^{14}\mathrm{C}/^{12}\mathrm{C}$ from a pre-bomb standard sample. Following Orr et al. (2017), the modeled tracer $^{14}\mathrm{DIC}^{\mathrm{abio}}$ is normalized by dividing by $^{14}r_{\mathrm{std}}$. Because it is abiotic and is not linked to biological carbon cycling, the modeled tracer $^{14}\mathrm{DIC}^{\mathrm{abio}}$ does not require a fractionation correction; therefore, given this implementation, $\Delta^{14}\mathrm{C}$ for the model is computed as

$$\Delta^{14}\mathrm{C} = 1000 \cdot \left({}^{14}\mathrm{DIC}^{\mathrm{abio}}/\mathrm{DIC}^{\mathrm{abio}} - 1 \right). \tag{14}$$

2.3 Numerical experiments

As mentioned above, the experiments described here are from the CESM2 contribution to CMIP6 (Eyring et al., 2016). We analyze 3 types of experiments: a preindustrial control experiment, experiments spanning the recent historical past, and future scenario experiments. In the preindustrial control experiment, referred to as piControl, prescribed forcings used by the model repeatedly cycle through values representative of the year 1850. The initialization of the piControl experiment is described below. The experiments of the recent historical past, referred to as historical, were run using prescribed forcings for years 1850–2014. These experiments were initialized from the piControl experiment, using the model's state at 1 January, taken from different years. We analyze

11 ensemble members of this type of experiment. The only difference between these ensemble members is the year of the piControl experiment that their initial state came from. The future scenario experiments follow the protocols of Scenario Model Intercomparison Project (ScenarioMIP) (O'Neill et al., 2016). The scenarios, referred to as Shared Socioeconomic Pathways (SSPs), were generated using integrated assessment models, based on a combination of different assumptions about societal development and target radiative forcings. We analyze 3 ensemble members of 4 different SSPs that span a range of anthropogenic impacts on the climate system. These experiments were initialized from the end of different historical experiments and were run, and used prescribed forcings, for years 2015-2100.

2.3.1 Initialization of piControl

To initialize the piControl, we applied a spin-up methodology to equilibrate biogeochemical tracers, including abiotic carbon and ideal age, to the simulated circulation. The spin-up was conducted using forcing and physical state extracted from a twenty-one year segment of a previous fully-coupled CESM2 experiment. The forcing was applied cyclically to the ocean and sea-ice component models for spin-up, which yields a much lower computational cost than the fully coupled system. The objective of the spin-up was to find a quasi-steady-state tracer distribution; this entails minimizing the difference in the tracer distributions between the beginning and end of the selected twenty-one year forcing period. The ocean physical state was reset at the beginning of each twenty-one year cycle, keeping it synchronized with the surface forcing and eliminating drift in temperature and salinity, for example. The spin-up was run for 1029 years. In the spin-up, the Ω_{crit} value (the threshold for $CaCO_3$ burial; see above) was manually adjusted at several points during the spin-up to ensure that loss of alkalinity from burial of $CaCO_3$ balanced riverine input of alkalinity. The final threshold value was 0.89, which was the value used in all subsequent experiments. Scaling coefficients applied to the burial of POM and silica at the seafloor (see above) were automatically adjusted in order to balance burial of carbon, phosphorus, and silicon with corresponding riverine inputs. All subsequent experiments used the values of the scaling factors determined in the spin-up. At several points during the spin-up, a Newton-Krylov based solver, based on (Lindsay, 2017), was used to more completely spin up a subset of the biogeochemical tracers. This Newton-Krylov based solver was applied to dissolved organic matter tracers (semi-labile and refractory), DIC, alkalinity, abiotic carbon tracers, and ideal age. The solver was not applied to other biogeochemical tracers because it had not yet been successfully extended to them. For each of tracers where it is applied, the Newton-Krylov approach solved directly for tracer equilibrium, assuming a fixed cyclo-stationary productivity field. The tracers to which the Newton-Krylov solver was applied are more equilibrated than one would expect from the duration of the spin-up. The globally-integrated air-sea CO_2 flux at the end of the spin-up was $\sim$0.02 Pg C yr^{-1}. The implication of this small air-sea CO_2 flux is that riverine inputs of carbon are nearly completely balanced by sediment burial.

3 Observational datasets

We used several observationally-based datasets for model validation. Model fields were averaged over the period 1990–2014, unless noted otherwise, and averaged across ensemble members to assess the simulated mean-state in comparison with observations. Model chlorophyll fields were compared to climatological seasonal chlorophyll means derived from the Sea-viewing Wide Field-of-view Sensor (SeaWiFS) satellite over the period September 1997 to December 2010, calculated using the GSM (Garver-Siegel-Maritorena model) algorithm (Maritorena et al., 2002; Maritorena & Siegel, 2005). We compared these to chlorophyll concentrations from the upper level of the ocean model (top 10 m). Modeled inorganic nutrient fields were compared those from the World Ocean Atlas version 2018 (WOA; Garcia et al., 2018). Observationally-based CFC and radiocarbon ($\Delta^{14}C$)

distributions were taken from the Global Ocean Data Analysis Project, version 1 (GLODAPv1) database (Key et al., 2004). The data comprising GLODAPv1 were collected over approximately the 1990s; thus, when comparing model output to these data, we use 11-yr, ensemble-mean averages centered on 1995. GLODAP reports constituent concentrations per mass of seawater. Since the CESM ocean component is volume conserving, we convert observation-based concentrations to per-volume units using a constant reference density, $\rho = 1026$ kg m^{-3} (no volume correction is applied to the radiocarbon isotope ratio). The simulated oceanic anthropogenic CO_2 (C_{ant}) inventory at year 2007 was compared to values derived from GLODAPv1 (Key et al., 2004; Sabine et al., 2004), with a correction for carbon uptake between 1994 and 2007 from Gruber et al. (2019). We compare 1990–2014 air-sea CO_2 flux to the gridded flux product of Landschützer et al. (2017), which we refer to as SOM-FFN, reflecting the two-step method described in Landschützer et al. (2016): first a self organizing map (SOM) is used to cluster the global ocean into biogeochemical provinces; second, a feed forward neural-network (FFN) is used to estimate pCO_2 from driver variables (i.e. sea surface temperature) after training using observations from the Surface Ocean CO_2 Atlas (SOCAT; Bakker et al., 2016). The SOM-FFN CO_2 fluxes are estimated from pCO_2 using the same gas exchange parameterization employed by MARBL (Sweeney et al., 2007) and wind speed derived from the National Centers for Environmental Prediction (Kalnay et al., 1996). To evaluate simulated dissolved iron (dFe) distributions, we make use of a data compilation extended from that in Moore and Braucher (2008) and including data from Tagliabue et al. (2012) and the GEOTRACES Intermediate Data Product compilation (Schlitzer et al., 2018). We compare simulated DOM distributions to a compilation of observations from Letscher and Moore (2015).

4 Results and discussion

In this section, we present and discuss several representative diagnostics of the CESM2 solutions submitted to CMIP6. Our objectives are not to provide a comprehensive analysis of these solutions, but rather we aim for a broad overview, illustrating key aspects of the ocean biogeochemical simulation and documenting important patterns in the model biases. We include a brief treatment of future projections, noting that output from CESM2 is also included in several model intercomparison papers (e.g., Séférian et al., 2020; Arora et al., 2020; Kwiatkowski et al., 2020).

4.1 Mixed layer depth

Surface mixed layer depths are a key control on the upper ocean habitat and important mediator of water mass ventilation affecting transient tracer uptake. The mixed layer depth simulation in CESM2 is therefore of interest in the context of understanding large-scale biogeochemical distributions and the strength of the biological pump. Notably, the mixed layer depth in the model manifests as a result of interactions between the vertical mixing scheme (Large et al., 1994) and both parameterized (e.g., Danabasoglu et al., 2010; Gent & Mcwilliams, 1990; Fox-Kemper et al., 2008) and resolved transport controlling stratification (Small et al., 2020). Figure 1 shows winter and summer distributions of mixed layer depth in CESM2 historical simulations compared with an observational estimate. To approximate the mixed layer depth, we use monthly-mean salinity and temperature to compute potential density; the mixed layer depth is calculated as the depth at which potential density changes by 0.125 kg m^{-3} from its surface value. The same procedure is applied to the World Ocean Atlas observationally-based product (Locarnini et al., 2019; Zweng et al., 2019). The model shows broad agreement with the observations in terms of the large-scale distribution of mixed layer depth (Figure 1 left two columns), but includes some important biases. Notably, high-latitude summertime mixed layers tend to be too deep in the model (Figure 1C), including regions with very deep biases in the North Atlantic and Southern Ocean. The wintertime mixed

Table 3. Global means fluxes.

Flux or Concentration	**preindustrial (CESM1)**	**1990 - 2014 (CESM1)**	**RCP 8.5 2090s (CESM1)**	**preindustrial (CESM2)**	**1990-2014 (CESM2)**	**SSP5-8.5 2090s (CESM2)**
Net primary production, full depth (PgC/yr)	55.9[a]	56.1[a]	54.0[a]	48.2	48.8	49.8
Sinking POC at 100 m (PgC/yr)	8.07	7.98	7.20	6.98	7.05	6.69
Sinking $CaCO_3$ at 100 m (PgC/yr)	0.757	0.748	0.723	0.767	0.767	0.808
Sinking SiO_2 at 100 m (Tmol/yr)	-	-	-	77.6	78.2	69.8
Rain ratio ($CaCO_3$/POC) at 100 m	0.094	0.094	0.100	0.110	0.109	0.121
Nitrogen fixation (TgN/yr)	175	169	144	241	243	285
Nitrogen deposition (TgN/yr)	6.6	29.6	30.0	13.3	37.2	38.3
Water Column Denitrification (TgN/yr)	190	194	188	185	192	256
Sediment Denitrification (TgN/yr)	-	-	-	67	71	68
Nitrogen Burial to Sediment (TgN/yr)	-	-	-	24	27	22
Nitrogen surface emissions (TgN/yr)	-	-	-	6	5	3
Nitrogen River Flux (TgN/yr)	-	-	-	13	25	25
N cycle imbalance [b] (TgN/yr)	-8.0	5.2	-13.8	-14.1	10.3	-0.8
Air-sea CO_2 flux (PgC/yr)	-0.02	2.03	4.71	-0.04	2.04	5.33
Diatom primary production, top 100m (%)	34	34	32	35	37	31
Diatom primary production, full depth (%)	35[a]	35[a]	32[a]	36	37	31

[a] NPP was only reported to 150m depth in CESM1

[b] Deposition + Fixation - Denitrification - Burial - Emissions + River Flux

layer depth distributions are characterized by heterogeneous biases in the North Atlantic (Figure 1F), though these biases are improved relative to older model versions (i.e., CCSM3) that lacked a parameterization of density driven overflows representing Denmark Strait and Faroe Bank Channel (Danabasoglu et al., 2012). Mixed layer depths are too shallow in the eastern Subpolar North Atlantic and Greenland, Iceland and Norwegian (GIN) Seas, but too deep in the Labrador Sea. Wintertime mixed layer depths are too shallow in the Subantarctic along the northern flank of the Antarctic Circumpolar Current (ACC) (Figure 1F). These biases are likely attributable to the representation of horizontal advection and insufficient transport of warm, salty subtropical waters into the ACC region (Small et al., 2020). The biases in the Subantarctic likely restrict Southern Ocean uptake of transient tracers (next section). Furthermore, the mixed layer depth simulation affects the seasonal evolution of NPP and air-sea CO_2 fluxes. For example, since iron is a critical control on Southern Ocean phytoplankton blooms, substantial biases in the mixed layer depth may result in poor simulation of iron supply, which is thought to be mediated largely by seasonal entrainment (Tagliabue et al., 2014).

4.2 Ventilation tracers

We examined the simulated distribution of three tracers: CFC-11, total radiocarbon (i.e., natural plus the "bomb-spike"; Δ^{14}C), and anthropogenic CO_2 (C_{ant}). CFC-11 and Δ^{14}C provide a means to assess the simulated circulation and potential biases in ventilation; as noted above, these tracers are simulated in the CESM2 ocean component, not within MARBL. However, we include them here as circulation biases provide an important context for understanding biogeochemical distributions. Since CFC-11 uptake is concentrated in water masses with ventilation ages of up to several decades (e.g., Dutay et al., 2002), biases in CFC-11 uptake are predominately informative of ventilation in thermocline waters. In order to isolate the influence of ventilation processes on CFC-11, we examine the partial pressure of CFC-11 (pCFC-11), thereby removing the influence of temperature and salinity biases on the tracer distribution. Δ^{14}C, by contrast, provides an indication of the fidelity of deep ocean overturning circulation on centennial timescales (e.g., Matsumoto, 2007). Rather than examine radiocarbon-derived estimates of circulation age, we simply present Δ^{14}C distributions directly as a qualitative indication of ventilation biases.

pCFC-11 highlights significant biases in thermocline ventilation in CESM2, with deficits in thermocline waters in both the Pacific and Atlantic basins (Figure 2C, F) and evidence of too much uptake in North Atlantic Deep Water (NADW; Figure 2C). These biases are largely similar to those found in CESM1 simulations (Long et al., 2013). Larger than observed values of Δ^{14}C are evident in the North Atlantic, confirming indications of vigorous NADW formation evident in pCFC-11 (Figure 3C). The most dramatic aspect of the ^{14}C simulation, however, is the very large Δ^{14}C deficit in the deep North Pacific (Figure 3F); this illustrates the sluggish circulation simulated by the coupled model in this region. As described above, the CESM2 simulation of ^{14}C is abiotic, so does not represent the vertical transfer of ^{14}C accomplished by sinking organic matter. The inclusion of biology would cause the simulated deep ocean Δ^{14}C to be less depleted, reducing the magnitude of the apparent bias; however, this effect is expected to quite small (e.g., 25‰) relative to the magnitude of the bias (Jahn et al., 2015). These deep circulation biases are much worse than in previous versions of the model (i.e., CESM1). Notably, testing indicates that running the CESM2 ocean component with reanalysis forcing restores the deep ocean circulation. Since changes to the physical ocean component between CESM1 and CESM2 were quite minimal, we thus attribute this bias to changes in the atmosphere component, though the specific mechanism remains under investigation. Oddly, Heuzé (2021) determined that CESM2 was one of the best performing models in terms of AABW and NADW formation; this study, however, was based on metrics of deep convection and watermass properties; it did not include an examination of transient tracers.

4.3 Anthropogenic CO_2 inventory

Ventilation tracers are useful in the context of understanding biases in the uptake of C_{ant}, since C_{ant} uptake is largely mediated by overturning circulation. To compute C_{ant}, we make use of the two parallel carbonate systems simulated by MARBL. In the CESM2 CMIP6 integrations, these tracer systems are subject to identical transport and source/sink terms; they differ only in their atmospheric CO_2 boundary conditions: the primary DIC tracer is exposed to increasing CO_2 according to historical or scenario forcing, while the secondary DIC tracer, "DIC_ALT_CO2", is forced with a constant preindustrial (1850) value for atmospheric CO_2 (284.7 ppm). We thus define anthropogenic CO_2 as

$$C_{ant} = \mathrm{DIC} - \mathrm{DIC\_ALT\_CO2}$$

Note that this definition differs subtly from subtracting a DIC field obtained from an 1850-control integration: changes in climate impact both DIC and DIC_ALT_CO2, so the resulting C_{ant} does not include the impact of climate on natural CO_2 as it would if the baseline DIC field were taken from an 1850-control integration. While climate impacts on natural CO_2 are significant under future scenarios with strong radiative forcing, this feedback is modest over the historical period.

CESM2 simulates weaker C_{ant} uptake than suggested by observational estimates (Figure 4). The model has C_{ant} deficiencies of order 10 mmol m^{-3} evident broadly in thermocline waters. The total GLODAP-based observational estimate for the C_{ant} inventory at year 2007 is 152±19 Pg C (Gruber et al., 2019; Sabine et al., 2004); the CESM2-simulated inventory at this time is 114 Pg C, or roughly 75% of the observations. Note that the GLODAP based observations to which we are comparing omit coverage in some oceanic regions (i.e., the Gulf of Mexico, the Arctic Ocean). The CESM2 simulated inventory for the portion of the ocean included in the gridded observational product is 106 Pg C at year 2007, compared with∼137 Pg C for the observationally-based C_{ant} estimates. A caveat with this comparison is that the model C_{ant} field only includes carbon uptake since 1850. As noted in Lindsay et al. (2014), Figure 3 of Khatiwala et al. (2009) indicates pre-1850 anthropogenic ocean uptake to be about 12±3 Pg C. Taking this into account reduces, but does not eliminate the model's low-uptake bias.

4.4 Macronutrients

A primary objective of MARBL is to represent the structure and function of the biological pump. The biological pump is fueled by nutrients; export of these constituents from the surface ocean via sinking and dissolved organic matter plays a dominant role in structuring nutrient distributions. Macronutrients are reasonably well-observed in the ocean and thus provide a good constraint on model performance. Figure 5 presents a comparison of surface NO_3, PO_4, and SiO_3 distributions from CESM2 with WOA observations. The overall geographical patterns of these macronutrients are well represented in CESM2, with increased surface nutrients at the high latitudes and equatorial regions and low nutrient concentrations in subtropical gyre regions. However, the simulated surface nutrient concentrations are too high in the subtropical oligotrophic gyres and too low in the Subarctic North Pacific; furthermore, there are substantial biases in the Southern Ocean. Simulated surface NO_3 and PO_4 are both too low in the Southern Ocean, by ∼4–8 mmol m^{-3} and ∼0.25–0.55 mmol m^{-3}, respectively. Conversely, SiO_3 concentrations are too low in the Antarctic zone and too high in the Subantarctic. Surface nutrients reflect the balance of net community production (NCP) and physical supply, which together determine the extent of nutrient utilization. Thus, negative biases in surface nutrients in the Southern Ocean suggest that the model may over estimate NCP and the simulated algal community composition includes an insufficient contribution from diatoms—or the Si to N stoichiometric ratio of diatom production, which is higher under extensive Fe limitation (Moore et al., 2004), may be too low. Alternatively, the nutrient content of water masses upwelling in the Southern Ocean may already be too low—indicative

of a large-scale bias in the nutrient simulation that may be related to excessive trapping of nutrient in the North Pacific.

A latitude-depth view of nutrient distributions lends credence to this latter hypothesis. Figures 6–8 show zonal-mean, depth-latitude plots of macronutrients in the Atlantic and Pacific Ocean basins, indicating how the vertical structure of the simulated macronutrients compares with observations. While the simulated nutrient distributions show overall structure that is similar to the observations, several key biases indicate deficiencies in the CESM2 solutions. Most notably, these include NO_3 depletion in the tropical thermocline (Figure 6C, F), which is driven by denitrification in overly extensive oxygen deficient zones, and excessive accumulation of macronutrients in the deep North Pacific, attributable to sluggish deep circulation in this region.

The vertical structure of PO_4 provides an indication of the functioning of the biological pump without the complications of denitrification; the zonal means of simulated PO_4 indicate excessive nutrient concentrations in the tropical thermocline, particularly in the Atlantic, and nutrient trapping the deep North Pacific (Figure 7). The negative bias in nitrate and phosphate in the Southern Ocean surface waters (Figure 5) is also evident in the ocean interior over much of the Southern Hemisphere water column (Figure 7C, F). This pattern demonstrates that the whole Southern Ocean nutrient inventory is too low in the model, suggesting that too weak supply of nutrients to the surface ocean via upwelling in this region is partially responsible for negative surface nutrient biases.

The situation is subtly different for silicate, which displays a positive surface bias over much of the Southern Ocean (Figure 5I)—but a dipole bias pattern in the zonal-mean column view (Figure 8C, F). This pattern is characterized by negative biases in the region associated with AABW and the deep overturning cell, but positive biases in upper, equatorward portion of the column associated with the upper cell and where Antarctic Intermediate Water and Subantarctic Mode water are formed. These patterns indicate that while SiO_3 supply via upwelling to Southern Ocean surface waters may be too weak, opal production is also too weak, resulting in excessive leakage of SiO_3 from the Southern Ocean (*sensu* Sarmiento et al., 2004). Sarmiento et al. (2007) demonstrated that the Southern Ocean effectively traps silica (see also Primeau et al., 2013; Moore et al., 2018), a phenomena we have also demonstrated operates in POP for $CaCO_3$ and alkalinity (Krumhardt et al., 2020). In this vein, excessive silica leakage from the Southern Ocean in CESM2 may help explain why upper-ocean SiO_3 concentrations are too high at the surface over much of the rest of the global ocean, with the exception of the North Pacific (Figure 8).

4.5 Nutrient limitation

Nutrients and temperature play important roles in structuring phytoplankton productivity throughout the global ocean. The most limiting nutrients for each phytoplankton functional type are shown in Figure 9; these fields are computed as phytoplankton-biomass-weighted means of the upper-ocean limitation terms, thereby providing a picture of resource limitation relevant to understanding vertically integrated production. Small phytoplankton in CESM2 are limited by N in much of the low to mid-latitudes, except in the South Pacific, where Fe is primarily limiting growth. Indeed Fe limits production of small phytoplankton and diatoms in most oceanic regions south of 15°S. These major patterns of phytoplankton N and Fe limitation are generally supported by observations (e.g., Moore et al., 2013). Diatoms are limited by SiO_3 in regions bordering the continents in the Southern Hemisphere, as well as in the North Pacific and North Atlantic in CESM2. Diazotrophs fix N and are therefore not limited by N availability; they are limited by Fe and P in the tropics and subtropics (Sañudo-Wilhelmy et al., 2001; Letscher & Moore, 2015); temperature limits the geographic distribution of diazotrophs to warmer

waters (>15°C; Figure 9C). P limitation is mainly evident in the low latitude North Atlantic for all three phytoplankton functional types; here increased Fe deposition from Saharan aeolian fluxes stimulate N fixation by diazotrophs making P the limiting nutrient (Wu et al., 2000; Sañudo-Wilhelmy et al., 2001).

4.6 Surface chlorophyll

Satellite-derived observations of chlorophyll provide a proxy for phytoplankton distribution and biomass. Here, we compare seasonal (DJF and JJA) mean chlorophyll concentrations from SeaWiFS to CESM2 chlorophyll concentrations in the surface ocean (Figure 10). While CESM2 simulates the overall patterns of chlorophyll distribution during the Southern Hemisphere growing season, it is markedly too high for certain regions (Figure 10A–C). Strong positive biases are evident in the Subantarctic region of the Southern Ocean, especially in the Atlantic sector and south of Australia. Chlorophyll concentrations in the eastern equatorial Pacific are also overestimated by CESM2. Despite a geographic pattern that is similar to the observations, Northern Hemisphere summer chlorophyll concentrations are also too high in the model for the North Pacific and North Atlantic, according to the SeaWiFS observations (Figure 10D–F). Another prevalent bias apparent in the model is in the coastal regions (Figure 10). Coastal phytoplankton production and chlorophyll concentrations are commonly underestimated in nominal 1-degree (or lower) resolution GCMs (Laufkötter et al., 2015)—though it is also the case that the satellite observations may overestimates chlorophyll in the coastal zone (e.g., Gregg & Casey, 2004).

4.7 Net primary productivity and export

Primary production by marine phytoplankton is the ultimate constraint on the strength of the biological pump and also forms the ecological base of the ocean food web. Satellite observation-based estimates of globally integrated net primary production (NPP) typically fall within the range of 43–67 Pg C year^{-1} (Behrenfeld et al., 2005; Behrenfeld & Falkowski, 1997). Globally integrated NPP in CESM2 is 48.9 Pg C yr^{-1} over the period 1990–2014 (Table 3, Figure 11), within the range of satellite-based estimates. The distribution of NPP in CESM2 follows a familiar pattern, with the highest rates of NPP in equatorial upwelling regions (Figure 11A); however, the NPP difference between the subtropics and extra-tropic appears less pronounced than that evident in satellite-based estimates (e.g., Behrenfeld et al., 2005). Simulated globally-integrated particulate export at 100 m for the same period is 7.1 Pg C yr^{-1} (Table 3, Figure 11), which is also broadly consistent with observationally-based estimates, considering uncertainty (e.g., Henson et al., 2011; Siegel et al., 2014; Boyd & Trull, 2007). The distribution of particulate export at 100 m has greater spatial variability than NPP (Figure 11B), as it reflects a combination of NPP and controls on export mediated by phytoplankton community composition. Indeed, the global mean particulate export ratio (pe-ratio = sinking export/NPP) in CESM2 is about 0.15, but varies by more than a factor of 3 (Figure 11C). Mineral ballasting by $CaCO_3$ and opal contributes to high pe-ratios (Armstrong et al., 2002; Lima et al., 2014), with the regions of high opal export, indicative of diatom-dominated assemblages, corresponding to the locations of high pe-ratio (Figure 12). Notably, the elemental composition of exported organic matter varies in MARBL. N:P concentrations are elevated below the subtropical oligotrophic gyres, which is broadly consistent with observations (e.g., Martiny et al., 2013) and inverse model results (Wang et al., 2019). These patterns are enabled by the variable P:C uptake ratios.

4.8 Air-sea CO_2 fluxes

Figure 13 shows a comparison of CESM2 simulated air-sea CO_2 (1990–2014), as well as an observationally-based flux estimate (Landschützer et al., 2017). In general,

the simulated flux field compares quite well with the observations (Figure 13A, B). The globally-integrated flux is larger in magnitude (-2.0 Pg C yr^{-1}) than in the observational product (-1.4 Pg C yr^{-1}), though this discrepancy is not significant if riverine carbon inputs are properly accounted for in the comparison. In nature, riverine carbon fluxes to the ocean induce net outgassing due to an imbalance between inputs and burial at the seafloor (Gruber et al., 2009); recent estimates suggest this flux is about 0.45–0.78 Pg C yr^{-1} (Resplandy et al., 2018). Recall from above, however, that the CESM2 spin-up methodology aimed to achieve a balance between riverine inputs and burial of carbon at the seafloor and near-zero net air-sea flux in the preindustrial state. Considering this methodology then, a correction for riverine fluxes would suggest that the model's simulated globally-integrated air-sea CO_2 flux is indistinguishable from that implied by the observations. The model simulates outgassing in the tropics, most notably in the equatorial Pacific, and CO_2 uptake at mid- and high-latitudes (Figure 13A, B). The seasonal cycle of zonal-mean CO_2 flux is also well simulated—though notable differences in the seasonal evolution of the fluxes are evident in the Southern Ocean poleward of 45°S (Figure 13C, D). This region is challenging to model, in part because the net air-sea CO_2 flux manifests as the residual between opposing thermal and biologically-driven tendencies (e.g., Mongwe et al., 2018).

4.9 Dissolved organic matter

A fraction of plankton loss terms are routed to the DOM pool, which is subsequently transported by circulation, and degraded by microbial activity. DOM thus provides a transport pathway for the export of biogeochemical constituents to the deep ocean. In particular, it is thought to account for ∼20% of total carbon export (Hansell, 2013). Indeed, in CESM2 DOC export across 100 m is 1.91 Pg C yr^{-1} during 1990–2014, which accounts for 21% of the total organic carbon flux across 100 m (particulate flux is 7.1 Pg C yr^{-1}, Figure 11B). Figure 14 shows upper 100 m total DOM (i.e., semi-labile plus refractory) concentrations simulated by CESM2 as well as observations of these constituents compiled by Letscher and Moore (2015). The distribution of DOM partially reflects surface water residence times, with high concentrations accumulating within the permanently stratified oligotrophic ocean and lower surface concentrations found within the equatorial and Southern Ocean upwelling regions. The simulated global maxima in surface DOC (76–96 µM) and DON (5.5–6.5 µM) concentrations are found in the tropical to subtropical Atlantic and Indian Ocean basins, in agreement with the observations. Simulated global maxima in surface DOP concentrations (0.23–0.28 µM) are found in the subtropical Pacific Ocean and northern Indian basin, while the global minimum is found in the subtropical North Atlantic Ocean (<0.08 µM), also in agreement with the observations. Important to capturing the global minimum in surface DOP within the subtropical North Atlantic is the ability for phytoplankton to use semi-labile DOP as a P source for growth when inorganic phosphate is scarce—as is the case for the North Atlantic subtropical gyre (Figure 5). Figure 15 presents two-dimensional histograms, showing the relationship between simulated and observed DOM. Very high observed DOM concentrations are likely to come from regions with significant riverine influence that may not be adequately captured by the model and the supplied riverine DOM forcing. The global-mean elemental composition of total DOM in CESM2 is 385:29:1 (C:N:P) in the upper 100 m, sampled at the same locations as the DOM observations, which have a mean elemental ratio of 735:60:1 (Letscher & Moore, 2015). This indicates that the MARBL DOM stoichiometry is P-enriched relative to the observations, while the simulated C:N stoichiometry is relative close to the observed values (MARBL C:N = 13.3; observed C:N = 12.3).

4.10 Nitrogen cycle

Globally-integrated nitrogen fixation over the 1990–2014 period averaged 243 Tg N yr^{-1} (Table 3, Figure 16A); this number is larger than observationally-based estimates,

which range from about 100–230 Tg N yr^{-1} (e.g., Zehr & Capone, 2021; Wang et al., 2019). Simulated water column and sedimentary denitrification over this period were 192 and 71 Tg N yr^{-1}, respectively. Burial of N at the sea floor and surface emissions of ammonia account for additional losses from the model, while atmospheric deposition and riverine inputs provide additional sources. Collectively, these terms lead to an N cycle imbalance of about 10 Tg N yr^{-1} (Table 3). Unfortunately, the CESM2 simulation of dissolved oxygen is inadequate (see above) strongly influencing simulated water-column denitrification; therefore, CESM2 cannot be reliably used to study changes to N cycle processes with climate.

4.11 Iron cycle

Figure 17 illustrates the spatial distribution of the dominant terms in the global ocean iron budget as simulated in CESM2. Iron is supplied to the ocean via prognostic atmospheric deposition (Figure 17A), with a pattern reflecting proximity to continental dust sources. The dominant source of iron to the ocean is from marine sediments (Figure 17B) with additional contributions from hydrothermal vents (Figure 17C). Riverine input of iron is small, accounting for only 0.37 Gmol yr^{-1}. Iron is removed from the ocean via burial at the seafloor (Figure 17D). The sources and sinks of dissolved iron in the ocean are highly uncertain and model intercomparison activities have demonstrated that it is possible to produce realistic dissolved iron concentration fields with very different inputs and loss terms (Tagliabue et al., 2016). Despite this caveat, there is useful information in a comparison of simulated dissolved iron concentrations to observations (Figures 18 and 19).

CESM2 captures the dominant structure of dissolved iron reasonably well, with elevated surface concentrations in the tropical Atlantic and much lower concentrations in the Pacific. Surface concentration of dissolved iron in the North Pacific appear to be too high in the model, which might be attributable to overly diffusive flow and unrealistic transport of sedimentary sources offshore. Indeed, we have found that iron supply in the North Pacific changes dramatically when integrating the model at high resolution (Harrison et al., 2018). Figure 19 shows global histograms of the model and observations; these plots indicate that CESM2 does a good job simulating the range of iron concentrations observed in the ocean, though does not have sufficient representation of waters with very low concentrations in the upper ocean. This bias is exacerbated at depth; below 500 m, the observations indicate that iron concentrations should be approximately normally-distributed with a median concentration of about 0.6 nM—but CESM2 simulates something closer to a uniform distribution (Figure 19C), which is likely tied to scavenging rates and ligand dynamics.

4.12 Transient simulations

Here we include a brief discussion of future scenario integrations conducted with CESM2. Space limitations preclude a comprehensive analysis, so we present only a few key metrics. Figure 20A shows the prescribed atmospheric CO_2 forcing for each of the future scenario integrations and Figure 20B illustrates the associated change in sea surface temperature (SST). The scenarios range from SSP1-2.6—under which CESM2 projects about 1.7°C of SST warming at 2100 relative to preindustrial—to SSP5-8.5, under which CESM2 projects SST warming of about 4.6°C. CESM2 has an equilibrium climate sensitivity (ECS, the change in surface temperature for a doubling of atmospheric CO_2 above preindustrial at equilibrium) of 5.2°C and—more relevant to the simulations at hand—a transient climate sensitivity (TCS, the surface temperature warming around the time of CO_2 doubling in a 1% per year CO_2 increase simulation) of 2.0°C. The CMIP6 multi-model mean for these quantities is 3.7±1.1 (standard deviation) for ECS and 2.0±0.4 for TSC (Meehl et al., 2020) and, indeed, CESM2 simulates transient warming close to the multi-model mean (Brunner et al., 2020). The transient behavior of globally-integrated

air-sea CO_2 flux is shown in Figure 20C as a function of time and Figure 20D as a function of atmospheric CO_2. Importantly, for the two high-CO_2 scenarios (SSP3-7.0 and SSP5-8.5), the ocean CO_2 uptake saturates (and under SSP5-8.5 even begins to decline), in spite of continually increasing atmospheric CO_2. This behavior is indicative of feedback; in particular, as the ocean carbon inventory increases, so does the Revelle Factor, limiting additional uptake (e.g., Schwinger et al., 2014). Furthermore, climate warming increases buoyancy stratification in the upper ocean, thereby reducing vertical exchange and the transfer of excess carbon into the ocean interior. Air-sea CO_2 flux in the two lower CO_2 scenarios (SSP1-2.6 and SSP2-4.5) shows somewhat distinct behavior, as these scenarios both include a reduction in the atmospheric CO_2 growth rate—in SSP1-2.6, there is actually a negative trend in atmospheric CO_2 beyond year 2070 (Figure 20A). As the atmospheric CO_2 forcing is relaxed, ocean CO_2 uptake declines; notably, in SSP1-2.6, this decline means that air-sea CO_2 uptake is weaker for the same atmospheric CO_2 mixing ratio than in the historical period (Figure 20D). This phenomenon has important implications for managing climate mitigation; CO_2 previously absorbed by the ocean drives hysteresis, meaning that the ocean sink will decline in efficiency as emissions-reductions slow the atmospheric growth rate.

The CESM2 transient integrations indicate contrasting projections for globally integrated NPP and export (Figure 21). NPP is simulated to increase over the historical period and continue increasing in the future, particularly under the high emission scenario SSP5-8.5. However, CESM2 projects a reduction in globally integrated POC flux at 100 m for all future scenarios (Figure 21B). These global changes reflect spatially heterogeneous patterns. The North Atlantic is projected to undergo strong reductions in NPP and export production, while NPP is projected to increase over much of the rest of the ocean (except in the western tropical Pacific and Indian basins) (Figure 22). Critically, shifts in algal community composition are a significant driver of changes in the pe-ratio. Globally, there is a decline in the pe-ratio under all warming scenarios, as well as a shift in algal community composition leading to diminished diatom prevalence relative to small phytoplankton. These changes are also spatially heterogeneous, however, as diatoms decline over most of the ocean except, most notably, in the Southern Ocean, where their relative prevalence increases dramatically (diatom fractions also increase in the equatorial Pacific) (Figure 22C, D). These patterns are broadly consistent with results from CMIP5, in which models capable of transitioning production from large phytoplankton (diatoms) to small phytoplankton projected only weak reductions in NPP, but significant changes in export (Fu et al., 2016; Bopp et al., 2013). As noted in Laufkötter et al. (2015), model differences in NPP reflect different choices in treatment of temperature sensitivity and model nutrient dynamics, linked to the sensitivity of nutrient supply to stratification. Most CMIP5 models projected decreasing globally integrated NPP ranging from -1% to -15% under RCP8.5 (Bopp et al., 2013); CMIP6 models do not show as much of a decline in NPP (Kwiatkowski et al., 2020).

5 Conclusion

We have presented a technical description of MARBL, which is the ocean biogeochemistry component for the CESM2. MARBL is a state-of-the-art global ocean biogeochemistry model, with a prognostic representation of the coupled cycles of nitrogen, phosphorus, silicon, iron, carbon and oxygen. The model is built on a plankton functional type paradigm, and supports flexible ecosystem configuration. In addition to documenting MARBL, we have presented and discussed diagnostics to evaluate the ocean biogeochemistry simulations in the fully-coupled CESM2 integrations submitted to CMIP6. Our analysis highlights challenges associated with the development and application of ocean biogeochemical models in the context of coarse resolution OGCMs. The CESM2 solutions suffer from weak thermocline ventilation, which produces overly extensive oxygen minimum zones and weakens uptake of transient tracers. Deep ocean circulation in CESM2

is also sluggish—so much so, in fact, that we had to artificially reduce oxygen consumption in the North Pacific to prevent widespread anoxia in the model. Unfortunately, the severity of this bias required several hundred years of integration to become clear, making it a challenging issue to address in the context of model development. While biases in circulation impose limits on the fidelity of model solutions, in general MARBL captures large-scale biogeochemical distributions reasonably well, and provides a platform for researching interactions between climate, nutrient and carbon cycling in the ocean.

MARBL has been explicitly designed to facilitate coupling with multiple OGCMs, an effort motivated in part by interest in engaging a broad research community. This capacity is being exercised currently: we presented solutions from MARBL integrated in POP2, and we have implemented MARBL in MOM6, the ocean component for CESM version 3; the Department of Energy has implemented MARBL in MPAS-O, the ocean component for the Energy Exascale Earth System Model (E3SM) (Burrows et al., 2020); efforts are underway to implement MARBL in the Regional Oceanographic Model (ROMS) (Shchepetkin & McWilliams, 2005), enabling high-resolution regional configurations; and finally, MARBL has been coupled to the Ocean Circulation Inverse Model (OCIM) (DeVries & Primeau, 2011; DeVries, 2014) leveraging an interface layer suitable for Matlab and Python applications. Future goals include establishing a one-dimensional test-bed framework, enabling more comprehensive parameter exploration and an educational resource. Our goals explicitly include building a diverse, inclusive community of researchers involved in the development and application of MARBL across a range of use-cases. Managing such a development process imposes some challenges, but also has the potential to yield significant benefits derived from synergies across diverse applications.

As mentioned above, the ecosystem configuration in MARBL is flexible, and improvements in the simulated phytoplankton and zooplankton diversity is currently an area of active development. Part of the motivation for this work is to improve the capacity for CESM to address critical questions related to the impacts of climate variability and change on marine ecosystems. Another area of interest involves climate intervention strategies, including the efficacy and potential impacts associated with ocean carbon dioxide removal (CDR) strategies.

In summary, we aim to continue to develop MARBL as a community resource and cutting-edge research tool. Work continues to improve MARBL, building toward a comprehensive treatment of ocean biogeochemical cycles, capable of robust assessments of climate impacts and the effect of human manipulations.

Acknowledgments

We acknowledge high-performance computing support from Cheyenne (doi:10.5065/D6RX99HX) provided by NCAR's Computational and Information Systems Laboratory, sponsored by the National Science Foundation (NSF). This material is based upon work supported by the National Center for Atmospheric Research, which is a major facility sponsored by the National Science Foundation under Cooperative Agreement No. 1852977. In addition to NSF funds to NCAR, MARBL development has been supported by the Office of Biological & Environmental Research (BER) within the Department of Energy (DOE) (DE-SC0012603). J.K.M. acknowledges support from DOE BER Earth System Modeling Program (DE-SC0016539). We gratefully acknowledge comments from Charles Stock on an early draft of this manuscript. Data from the CESM simulations performed for this study are available via the Climate Data Gateway (https://www.earthsystemgrid.org) in native output format as well as in CMIP standard format via the Earth System Grid Federation (https://esgf.llnl.gov).

References

Adcroft, A., Anderson, W., Balaji, V., Blanton, C., Bushuk, M., Dufour, C. O., ... et al. (2019). The GFDL global ocean and sea ice model OM4.0: Model description and simulation features. *Journal of Advances in Modeling Earth Systems*. doi: 10.1029/2019ms001726

Anderson, L. A., & Sarmiento, J. L. (1994, Mar). Redfield ratios of remineralization determined by nutrient data analysis. *Global Biogeochem. Cycles*, *8*(1), 65–80. Retrieved from http://dx.doi.org/10.1029/93GB03318 doi: 10.1029/93gb03318

Armstrong, R., Lee, C., Hedges, J., Honjo, S., & Wakeham, S. (2002). A new, mechanistic model for organic carbon fluxes in the ocean based on the quantitative association of POC with ballast minerals. *Deep-Sea Res.*, *49*(1–3), 219–236. doi: 10.1016/S0967-0645(01)00101-1

Arora, V. K., Katavouta, A., Williams, R. G., Jones, C. D., Brovkin, V., Friedlingstein, P., ... Ziehn, T. (2020). Carbon–concentration and carbon–climate feedbacks in CMIP6 models and their comparison to CMIP5 models. *Biogeosciences*, *17*(16), 4173–4222. Retrieved from https://bg.copernicus.org/articles/17/4173/2020/ doi: 10.5194/bg-17-4173-2020

Azam, F., Fenchel, T., Field, J. G., Gray, J. S., Meyer-Reil, L. A., & Thingstad, F. (1983). The ecological role of water-column microbes in the sea. *Marine Ecology Progress Series*, *10*(3), 257–263.

Bakker, D. C. E., Pfeil, B., Landa, C. S., Metzl, N., O'Brien, K. M., Olsen, A., ... Xu, S. (2016, September). A multi-decade record of high-quality fco_2 data in version 3 of the surface ocean CO_2 atlas (SOCAT). *Earth system science data*, *8*(2), 383–413. doi: 10.5194/essd-8-383-2016

Behrenfeld, M. J., Boss, E., Siegel, D. A., & Shea, D. M. (2005). Carbon-based ocean productivity and phytoplankton physiology from space. *Global Biogeochem. Cycles*, *19*(1). Retrieved from https://agupubs.onlinelibrary.wiley.com/doi/abs/10.1029/2004GB002299 doi: 10.1029/2004GB002299

Behrenfeld, M. J., & Falkowski, P. G. (1997). Photosynthetic rates derived from satellite-based chlorophyll concentration. *Limnology and Oceanography*, *42*(1), 1-20. Retrieved from https://aslopubs.onlinelibrary.wiley.com/doi/abs/10.4319/lo.1997.42.1.0001 doi: 10.4319/lo.1997.42.1.0001

Beusen, A. H. W., Bouwman, A. F., Van Beek, L. P. H., Mogollón, J. M., & Middelburg, J. J. (2016). Global riverine N and P transport to ocean increased during the 20th century despite increased retention along the aquatic continuum. *Biogeosciences*, *13*, 2441-2451. doi: 10.5194/bg-13-2441-2016

Beusen, A. H. W., Van Beek, L. P. H., Bouwman, A. F., Mogollón, J. M., & Middelburg, J. J. (2015). Coupling global models for hydrology and nutrient loading to simulate nitrogen and phosphorus retention in surface water – description of IMAGE–GNM and analysis of performance. *Geosci. Model Dev.*, *8*(12), 4045–4067. doi: 10.5194/gmd-8-4045-2015

Bohlen, L., Dale, A. W., & Wallmann, K. (2012, Sep). Simple transfer functions for calculating benthic fixed nitrogen losses and C:N:P regeneration ratios in global biogeochemical models. *Global Biogeochem. Cycles*, *26*(3). Retrieved from http://dx.doi.org/10.1029/2011GB004198 doi: 10.1029/2011gb004198

Bopp, L., Resplandy, L., Orr, J. C., Doney, S. C., Dunne, J. P., Gehlen, M., ... Vichi, M. (2013). Multiple stressors of ocean ecosystems in the 21st century: projections with CMIP5 models. *Biogeosciences*, *10*, 6225-6245. doi: 10.5194/bg-10-6225-2013

Boyd, P. W., & Trull, T. W. (2007, March). Understanding the export of biogenic particles in oceanic waters: Is there consensus? *Progress in oceanography*, *72*(4), 276–312. doi: 10.1016/j.pocean.2006.10.007

Brunner, L., Pendergrass, A. G., Lehner, F., Merrifield, A. L., Lorenz, R., & Knutti, R. (2020, November). Reduced global warming from CMIP6 projections when

weighting models by performance and independence. *Earth system dynamics*, *11*(4), 995–1012. doi: 10.5194/esd-11-995-2020

Burrows, S. M., Maltrud, M., Yang, X., Zhu, Q., Jeffery, N., Shi, X., ... Leung, L. R. (2020, September). The DOE E3SM v1.1 biogeochemistry configuration: Description and simulated ecosystemclimate responses to historical changes in forcing. *Journal of Advances in Modeling Earth Systems*, *12*(9). doi: 10.1029/2019ms001766

Collins, W. D., Bitz, C. M., Blackmon, M. L., Bonan, G. B., Bretherton, C. S., Carton, J. A., ... et al. (2006). The Community Climate System Model Version 3 (CCSM3). *Journal of Climate*, *19*(11), 2122–2143. doi: 10.1175/jcli3761.1

Danabasoglu, G., Bates, S. C., Briegleb, B. P., Jayne, S. R., Jochum, M., Large, W. G., ... Yeager, S. G. (2012). The CCSM4 Ocean Component. *Journal of Climate*, *25*(5), 1361-1389. doi: 10.1175/JCLI-D-11-00091.1

Danabasoglu, G., Lamarque, J. ., Bacmeister, J., Bailey, D. A., DuVivier, A. K., Edwards, J., ... Strand, W. G. (2020, February). The Community Earth System Model version 2 (CESM2). *Journal of Advances in Modeling Earth Systems*, *12*(2). doi: 10.1029/2019ms001916

Danabasoglu, G., Large, W. G., & Briegleb, B. P. (2010). Climate impacts of parameterized Nordic Sea overflows. *Journal of Geophysical Research: Oceans (19782012)*, *115*(C11). doi: 10.1029/2010JC006243

DeVries, T. (2014, July). The oceanic anthropogenic CO_2 sink: Storage, air-sea fluxes, and transports over the industrial era. *Global Biogeochem. Cycles*, *28*(7), 631–647. doi: 10.1002/2013GB004739

DeVries, T., & Primeau, F. (2011, December). Dynamically and observationally constrained estimates of Water-Mass distributions and ages in the global ocean. *Journal of physical oceanography*, *41*(12), 2381–2401. doi: 10.1175/JPO-D-10-05011.1

Doney, S., Lima, I., Feely, R., Glover, D., Lindsay, K., Mahowald, N., ... Wanninkhof, R. (2009). Mechanisms governing interannual variability in upper-ocean inorganic carbon system and air-sea CO_2 fluxes: physical climate and atmospheric dust. *Deep Sea Res., Part II*, *56*(8–10), 640-655. doi: 10.1016/j.dsr2.2008.12.006

Doney, S. C., Glover, D. M., & Najjar, R. G. (1996). A new coupled, one-dimensional biological-physical model for the upper ocean: Applications to the JGOFS Bermuda Atlantic Time-series Study (BATS) site. *Deep Sea Research Part II: Topical Studies in Oceanography*, *43*(2-3), 591–624. doi: 10.1016/0967-0645(95)00104-2

Doney, S. C., Lindsay, K., Caldeira, K., Campin, J.-M., Drange, H., Dutay, J.-C., ... Yool, A. (2004, September). Evaluating global ocean carbon models: The importance of realistic physics. *Global Biogeochem. Cycles*, *18*(3). doi: 10.1029/2003gb002150

Doney, S. C., Mahowald, N., Lima, I., Feely, R. A., Mackenzie, F. T., Lamarque, J.-F., & Rasch, P. J. (2007). Impact of anthropogenic atmospheric nitrogen and sulfur deposition on ocean acidification and the inorganic carbon system. *Proceedings of the National Academy of Sciences*, *104*(37), 14580–14585. doi: 10.1073/pnas.0702218104

Dunne, J. P., Sarmiento, J. L., & Gnanadesikan, A. (2007, Oct). A synthesis of global particle export from the surface ocean and cycling through the ocean interior and on the seafloor. *Global Biogeochem. Cycles*, *21*(4). Retrieved from http://dx.doi.org/10.1029/2006GB002907 doi: 10.1029/2006gb002907

Dutay, J.-C., Bullister, J. L., Doney, S. C., Orr, J. C., Najjar, R., Caldeira, K., ... Yool, A. (2002, January). Evaluation of ocean model ventilation with CFC-11: comparison of 13 global ocean models. *Ocean Modelling*, *4*(2), 89–120. doi: 10.1016/S1463-5003(01)00013-0

Eddebbar, Y. A., Rodgers, K. B., Long, M. C., Subramanian, A. C., Xie, S.-P., &

Keeling, R. F. (2019). El Niño–Like Physical and Biogeochemical Ocean Response to Tropical Eruptions. *Journal of Climate*, *32*(9), 2627–2649. doi: 10.1175/jcli-d-18-0458.1

Eyring, V., Bony, S., Meehl, G. A., Senior, C. A., Stevens, B., Stouffer, R. J., & Taylor, K. E. (2016). Overview of the Coupled Model Intercomparison Project phase 6 (CMIP6) experimental design and organization. *Geosci. Model Dev.*, *9*(5), 1937–1958. doi: 10.5194/gmd-9-1937-2016

Fasham, M. (1995). Variations in the seasonal cycle of biological production in subarctic oceans: A model sensitivity analysis. *Deep Sea Research Part I: Oceanographic Research Papers*, *42*(7), 1111-1149. Retrieved from https://www.sciencedirect.com/science/article/pii/096706379500054A doi: https://doi.org/10.1016/0967-0637(95)00054-A

Fox-Kemper, B., Ferrari, R., & Hallberg, R. (2008). Parameterization of mixed layer eddies. Part I: Theory and diagnosis. *Journal of Physical Oceanography*, *38*(6), 1145–1165. doi: 10.1175/2007JPO3792.1

Friedlingstein, P., Cox, P., Betts, R., Bopp, L., von Bloh, W., Brovkin, V., … Zeng, N. (2006). Climate-carbon cycle feedback analysis: Results from the C^4MIP model intercomparison. *Journal of Climate*, *19*(14), 3337-3353. doi: 10.1175/JCLI3800.1

Fu, W., Randerson, J. T., & Moore, J. K. (2016, September). Climate change impacts on net primary production (NPP) and export production (EP) regulated by increasing stratification and phytoplankton community structure in the CMIP5 models. *Biogeosciences*, *13*(18), 5151–5170. doi: 10.5194/bg-13-5151-2016

Galbraith, E. D., & Martiny, A. C. (2015). A simple nutrient-dependence mechanism for predicting the stoichiometry of marine ecosystems. *Proc. Natl. Acad. Sci. U.S.A.*, *112*(27), 8199–8204. doi: 10.1073/pnas.1423917112

Gangstø, R., Gehlen, M., Schneider, B., Bopp, L., Aumont, O., & Joos, F. (2008). Modeling the marine aragonite cycle: changes under rising carbon dioxide and its role in shallow water $CaCO_3$ dissolution. *Biogeosciences*, *5*(4), 1057–1072. doi: 10.5194/bg-5-1057-2008

Garcia, H. E., Weathers, K., Paver, C. R., Smolyar, I., Boyer, T. P., Locarnini, R. A., … Reagan, J. R. (2018). *World Ocean Atlas 2018, Volume 4: Dissolved inorganic nutrients (phosphate, nitrate and nitrate+nitrite, silicate)* (Vol. NOAA Atlas NESDIS 84). U.S. Department of Commerce. Retrieved from https://www.ncei.noaa.gov/access/world-ocean-atlas-2018/

Geider, R. J., MacIntyre, H. L., & Kana, T. M. (1997). Dynamic model of phytoplankton growth and acclimation: responses of the balanced growth rate and the chlorophyll a: carbon ratio to light, nutrient-limitation and temperature. *Marine Ecology Progress Series*, *148*(1/3), 187–200.

Geider, R. J., Maclntyre, H. L., & Kana, T. M. (1998, Jun). A dynamic regulatory model of phytoplanktonic acclimation to light, nutrients, and temperature. *Limnology and Oceanography*, *43*(4), 679–694. Retrieved from http://dx.doi.org/10.4319/lo.1998.43.4.0679 doi: 10.4319/lo.1998.43.4.0679

Gent, P. R., & Mcwilliams, J. C. (1990, January). Isopycnal mixing in ocean circulation models. *Journal of physical oceanography*, *20*(1), 150–155. doi: 10.1175/1520-0485(1990)020⟨0150:IMIOCM⟩2.0.CO;2

Gregg, W. W., & Casey, N. W. (2004, December). Global and regional evaluation of the SeaWiFS chlorophyll data set. *Remote sensing of environment*, *93*(4), 463–479. doi: 10.1016/j.rse.2003.12.012

Gruber, N., Clement, D., Carter, B. R., Feely, R. A., van Heuven, S., Hoppema, M., … et al. (2019). The oceanic sink for anthropogenic CO_2 from 1994 to 2007. *Science*, *363*(6432), 1193–1199. doi: 10.1126/science.aau5153

Gruber, N., Gloor, M., Mikaloff Fletcher, S. E., Doney, S. C., Dutkiewicz, S., Follows, M. J., … Others (2009). Oceanic sources, sinks, and transport of

atmospheric CO_2. *Global biogeochemical cycles*, *23*(1).

Han, Q., Moore, J. K., Zender, C., Measures, C., & Hydes, D. (2008). Constraining oceanic dust deposition using surface ocean dissolved Al. *Global Biogeochem. Cycles*, *22*(2). doi: 10.1029/2007gb002975

Hansell, D. A. (2013). Recalcitrant dissolved organic carbon fractions. *Annual review of marine science*, *5*, 421–445. doi: 10.1146/annurev-marine-120710-100757

Harrison, C. S., Long, M. C., Lovenduski, N. S., & Moore, J. K. (2018, April). Mesoscale effects on carbon export: A global perspective. *Global Biogeochem. Cycles*, *32*(4), 680–703. doi: 10.1002/2017gb005751

Henson, S. A., Sanders, R., Madsen, E., Morris, P. J., Le Moigne, F., & Quartly, G. D. (2011, February). A reduced estimate of the strength of the ocean's biological carbon pump. *Geophysical research letters*, *38*(4). doi: 10.1029/2011gl046735

Heuzé, C. (2021, January). Antarctic bottom water and north atlantic deep water in CMIP6 models. *Ocean Science*, *17*(1), 59–90. doi: 10.5194/os-17-59-2021

Holligan, P., Charalampopoulou, A., & Hutson, R. (2010). Seasonal distributions of the coccolithophore, Emiliania huxleyi, and of particulate inorganic carbon in surface waters of the Scotia Sea. *Journal of Marine Systems*, *82*(4), 195 - 205. doi: http://dx.doi.org/10.1016/j.jmarsys.2010.05.007

Iglesias-Rodríguez, M. D., Brown, C. W., Doney, S. C., Kleypas, J., Kolber, D., Kolber, Z., ... Falkowski, P. G. (2002). Representing key phytoplankton functional groups in ocean carbon cycle models: Coccolithophorids. *Global Biogeochemical Cycles*, *16*(4), 47-1–47-20. (1100) doi: 10.1029/2001GB001454

Jahn, A., Lindsay, K., Giraud, X., Gruber, N., Otto-Bliesner, B. L., Liu, Z., & Brady, E. C. (2015, August). Carbon isotopes in the ocean model of the Community Earth System Model (CESM1). *Geosci. Model Dev.*, *8*(8), 2419–2434. doi: 10.5194/gmd-8-2419-2015

Jones, C., Robertson, E., Arora, V., Friedlingstein, P., Shevliakova, E., Bopp, L., ... et al. (2013, Jul). Twenty-first-century compatible CO_2 emissions and airborne fraction simulated by CMIP5 earth system models under four representative concentration pathways. *Journal of Climate*, *26*(13), 4398–4413. Retrieved from http://dx.doi.org/10.1175/JCLI-D-12-00554.1 doi: 10.1175/jcli-d-12-00554.1

Kalnay, E., Kanamitsu, M., Kistler, R., Collins, W., Deaven, D., Gandin, L., ... Joseph, D. (1996, March). The NCEP/NCAR 40-year reanalysis project. *Bulletin of the American Meteorological Society*, *77*(3), 437–472. doi: 10.1175/1520-0477(1996)077⟨0437:TNYRP⟩2.0.CO;2

Kay, J. E., Deser, C., Phillips, A., Mai, A., Hannay, C., Strand, G., ... et al. (2015). The Community Earth System Model (CESM) large ensemble project: A community resource for studying climate change in the presence of internal climate variability. *Bulletin of the American Meteorological Society*, *96*(8), 1333–1349. doi: 10.1175/bams-d-13-00255.1

Key, R., Kozyr, A., Sabine, C., Lee, K., Wanninkhof, R., Bullister, J., ... Peng, T. (2004). A global ocean carbon climatology: Results from Global Data Analysis Project (GLODAP). *Global Biogeochem. Cycles*, *18*(4). doi: 10.1029/2004GB002247

Khatiwala, S., Primeau, F., & Hall, T. (2009). Reconstruction of the history of anthropogenic CO_2 concentrations in the ocean. *Nature*, *462*(7271), 346–349. doi: 10.1038/nature08526

Krishnamurthy, A., Moore, J., Mahowald, N., Luo, C., Doney, S., Lindsay, K., & Zender, C. (2009). Impacts of increasing anthropogenic soluble iron and nitrogen deposition on ocean biogeochemistry. *Global Biogeochem. Cycles*, *23*(3). doi: 10.1029/2008GB003440

Krishnamurthy, A., Moore, J. K., Mahowald, N., Luo, C., & Zender, C. S. (2010).

Impacts of atmospheric nutrient inputs on marine biogeochemistry. *Journal of Geophysical Research*, *115*(G1). doi: 10.1029/2009jg001115

Krishnamurthy, A., Moore, J. K., Zender, C. S., & Luo, C. (2007). Effects of atmospheric inorganic nitrogen deposition on ocean biogeochemistry. *J. Geophys. Res.*, *112*(G2). doi: 10.1029/2006JG000334

Krumhardt, K. M., Long, M. C., Lindsay, K., & Levy‘, M. N. (2020, December). Southern ocean calcification controls the global distribution of alkalinity. *Global biogeochemical cycles*, *34*(12). doi: 10.1029/2020gb006727

Krumhardt, K. M., Lovenduski, N. S., Iglesias-Rodriguez, M. D., & Kleypas, J. A. (2017). Coccolithophore growth and calcification in a changing ocean. *Progress in Oceanography*, *159*, 276–295. doi: 10.1016/j.pocean.2017.10.007

Krumhardt, K. M., Lovenduski, N. S., Long, M. C., Levy, M., Lindsay, K., Moore, J. K., & Nissen, C. (2019). Coccolithophore growth and calcification in an acidified ocean: Insights from Community Earth System Model simulations. *Journal of Advances in Modeling Earth Systems*, *11*(5), 1418–1437. doi: 10.1029/2018ms001483

Krumhardt, K. M., Lovenduski, N. S., Long, M. C., Luo, J. Y., Lindsay, K., Yeager, S., & Harrison, C. (2020, June). Potential predictability of net primary production in the ocean. *Global Biogeochem. Cycles*, *34*(6), e2020GB006531. doi: 10.1029/2020GB006531

Kwiatkowski, L., Torres, O., Bopp, L., Aumont, O., Chamberlain, M., Christian, J. R., ... Ziehn, T. (2020). Twenty-first century ocean warming, acidification, deoxygenation, and upper-ocean nutrient and primary production decline from CMIP6 model projections. *Biogeosciences*, *17*(13), 3439–3470. Retrieved from https://bg.copernicus.org/articles/17/3439/2020/ doi: 10.5194/bg-17-3439-2020

Landschützer, P., Gruber, N., & Bakker, D. C. E. (2016). Decadal variations and trends of the global ocean carbon sink. *Global Biogeochem. Cycles*, *30*(10), 1396–1417. doi: 10.1002/2015gb005359

Landschützer, P., Max Planck Institute For Meteorology-Hamburg (MPI), Gruber, N., Institute Of Biogeochemistry And Pollutant Dynamics (IBP), Bakker, D. C. E., & University Of East Anglia; School Of Environmental Sciences. (2017). *An observation-based global monthly gridded sea surface pCO_2 product from 1982 onward and its monthly climatology (NCEI accession 0160558).* NOAA National Centers for Environmental Information. doi: 10.7289/V5Z899N6

Large, W. G., McWilliams, J. C., & Doney, S. C. (1994). Oceanic vertical mixing: A review and a model with a nonlocal boundary layer parameterization. *Reviews of geophysics*, *32*(4), 363. doi: 10.1029/94rg01872

Laufkötter, C., Vogt, M., Gruber, N., Aita-Noguchi, M., Aumont, O., Bopp, L., ... Völker, C. (2015). Drivers and uncertainties of future global marine primary production in marine ecosystem models. *Biogeosciences*, *12*(23), 6955–6984. Retrieved from https://www.biogeosciences.net/12/6955/2015/ doi: 10.5194/bg-12-6955-2015

Letscher, R. T., & Moore, J. K. (2015, Mar). Preferential remineralization of dissolved organic phosphorus and non-redfield dom dynamics in the global ocean: Impacts on marine productivity, nitrogen fixation, and carbon export. *Global Biogeochem. Cycles*, *29*(3), 325–340. Retrieved from http://dx.doi.org/10.1002/2014GB004904 doi: 10.1002/2014gb004904

Letscher, R. T., Moore, J. K., Teng, Y.-C., & Primeau, F. (2015, Jan). Variable C : N : P stoichiometry of dissolved organic matter cycling in the Community Earth System Model. *Biogeosciences*, *12*(1), 209–221. Retrieved from http://dx.doi.org/10.5194/bg-12-209-2015 doi: 10.5194/bg-12-209-2015

Lima, I. D., Lam, P. J., & Doney, S. C. (2014). Dynamics of particulate organic carbon flux in a global ocean model. *Biogeosciences*, *11*(4), 1177–1198. doi: 10

.5194/bg-11-1177-2014

Lindsay, K. (2017). A Newton-Krylov solver for fast spin-up of online ocean tracers. *Ocean Modelling*, *109*, 33–43. doi: 10.1016/j.ocemod.2016.12.001

Lindsay, K., Bonan, G., Doney, S. C., Hoffman, F., Lawrence, D. M., Long, M. C., ... Thornton, P. E. (2014). Preindustrial control and 20th Century experiments with the earth system model CESM1(BGC). *J. Clim.*, *27*(24), 8981-9005. doi: 10.1175/JCLI-D-12-00565.1

Locarnini, R. A., Mishonov, A. V., Baranova, O. K., Boyer, T. P., Zweng, M. M., Garcia, H. E., ... Smolyar, I. (2019). *World Ocean Atlas 2018, Volume 1: Temperature* (Vol. NOAA Atlas NESDIS 81). U.S. Department of Commerce. Retrieved from http://www.nodc.noaa.gov/OC5/indprod.html

Long, M. C., Deutsch, C. A., & Ito, T. (2016). Finding forced trends in oceanic oxygen. *Global Biogeochem. Cycles*, *30*. doi: 10.1002/2015GB005310

Long, M. C., Lindsay, K., & Holland, M. M. (2015). Modeling photosynthesis in sea ice covered waters. *J. Adv. Model. Earth Syst.*, *07*(3), 1189-1206. doi: 10.1002/2015MS000436

Long, M. C., Lindsay, K., Peacock, S., Moore, J. K., & Doney, S. C. (2013). Twentieth-century oceanic carbon uptake and storage in CESM1(BGC). *Journal of Climate*, *26*(18), 6775–6800. doi: 10.1175/jcli-d-12-00184.1

Lovenduski, N. S., Gruber, N., & Doney, S. C. (2008). Toward a mechanistic understanding of the decadal trends in the Southern Ocean carbon sink. *Global Biogeochem. Cycles*, *22*(3). doi: 10.1029/2007gb003139

Lovenduski, N. S., Long, M. C., & Lindsay, K. (2015). Natural variability in the surface ocean carbonate ion concentration. *Biogeosciences*, *12*, 6321-6335. doi: 10.5194/bg-12-6321-2015

Lovenduski, N. S., McKinley, G. A., Fay, A. R., Lindsay, K., & Long, M. C. (2016). Partitioning uncertainty in ocean carbon uptake projections: Internal variability, emission scenario, and model structure. *Global Biogeochem. Cycles*, *30*, 1276-1287. doi: 10.1002/2016GB005426

Lovenduski, N. S., Yeager, S. G., Lindsay, K., & Long, M. C. (2019). Predicting near-term variability in ocean carbon uptake. *Earth System Dynamics*, *10*(1), 45–57. doi: 10.5194/esd-10-45-2019

Mahowald, N., Lindsay, K., Rothenberg, D., Doney, S. C., Moore, J. K., Thornton, P., ... Jones, C. D. (2011). Desert dust and anthropogenic aerosol interactions in the Community Climate System Model coupled-carbon-climate model. *Biogeosciences*, *8*(2), 387–414. doi: 10.5194/bg-8-387-2011

Marinov, I., Doney, S. C., & Lima, I. D. (2010). Response of ocean phytoplankton community structure to climate change over the 21st century: partitioning the effects of nutrients, temperature and light. *Biogeosciences*, *7*, 3941-3959. doi: 10.5194/bg-7-3941-2010

Maritorena, S., & Siegel, D. A. (2005, February). Consistent merging of satellite ocean color data sets using a bio-optical model. *Remote sensing of environment*, *94*(4), 429–440. doi: 10.1016/j.rse.2004.08.014

Maritorena, S., Siegel, D. A., & Peterson, A. R. (2002, May). Optimization of a semianalytical ocean color model for global-scale applications. *Applied optics*, *41*(15), 2705–2714. doi: 10.1364/ao.41.002705

Martiny, A. C., Pham, C. T. A., Primeau, F. W., Vrugt, J. A., Keith Moore, J., Levin, S. A., & Lomas, M. W. (2013, March). Strong latitudinal patterns in the elemental ratios of marine plankton and organic matter. *Nature geoscience*, *6*(4), 279–283. doi: 10.1038/ngeo1757

Matsumoto, K. (2007, September). Radiocarbon-based circulation age of the world oceans. *Journal of geophysical research*, *112*(C9). doi: 10.1029/2007jc004095

Mayorga, E., Seitzinger, S. P., Harrison, J. A., Dumont, E., Beusen, A. H., Bouwman, A., ... Van Drecht, G. (2010). Global Nutrient Export from WaterSheds 2 (NEWS 2): Model development and implementation. *Environ. Model. Softw.*,

25(7), 837–853. doi: 10.1016/j.envsoft.2010.01.007

McKinley, G. A., Pilcher, D. J., Fay, A. R., Lindsay, K., Long, M. C., & Lovenduski, N. (2016). Timescales for detection of trends in the ocean carbon sink. *Nature*, *530*, 469–472. doi: 10.1038/nature16958

Meehl, G. A., Senior, C. A., Eyring, V., Flato, G., Lamarque, J.-F., Stouffer, R. J., ... Schlund, M. (2020, June). Context for interpreting equilibrium climate sensitivity and transient climate response from the CMIP6 earth system models. *Science advances*, *6*(26), eaba1981. doi: 10.1126/sciadv.aba1981

Mongwe, N. P., Vichi, M., & Monteiro, P. M. S. (2018, May). The seasonal cycle of $p\mathrm{CO}_2$ and CO_2 fluxes in the Southern Ocean: diagnosing anomalies in CMIP5 earth system models. *Biogeosciences*, *15*(9), 2851–2872. doi: 10.5194/bg-15-2851-2018

Monterey, G., & Levitus, S. (1997). *Seasonal variability of mixed layer depth for the world ocean* (Vol. NOAA Atlas NESDIS 14). U.S. Department of Commerce.

Moore, C. M., Mills, M. M., Arrigo, K. R., Berman-Frank, I., Bopp, L., Boyd, P. W., ... Ulloa, O. (2013). Processes and patterns of oceanic nutrient limitation. *Nature Geoscience*, *6*(9), 701–710. Retrieved from https://doi.org/10.1038/ngeo1765 doi: 10.1038/ngeo1765

Moore, J. K., & Braucher, O. (2008). Sedimentary and mineral dust sources of dissolved iron to the world ocean. *Biogeosciences*, *5*(3), 631-656. doi: 10.5194/bg-5-631-2008

Moore, J. K., & Doney, S. C. (2007). Iron availability limits the ocean nitrogen inventory stabilizing feedbacks between marine denitrification and nitrogen fixation. *Global Biogeochem. Cycles*, *21*. doi: 10.1029/2006GB002762

Moore, J. K., Doney, S. C., Glover, D. M., & Fung, I. Y. (2002a). Iron cycling and nutrient-limitation patterns in surface waters of the World Ocean. *Deep Sea Res., Part II*, *49*, 463-507. doi: 10.1016/S0967-0645(01)00109-6

Moore, J. K., Doney, S. C., Kleypas, J. A., Glover, D. M., & Fung, I. Y. (2002). An intermediate complexity marine ecosystem model for the global domain. *Deep Sea Res.*, *49*(1–3), 403–462. doi: 10.1016/S0967-0645(01)00108-4

Moore, J. K., Doney, S. C., & Lindsay, K. (2004). Upper ocean ecosystem dynamics and iron cycling in a global three-dimensional model. *Global Biogeochem. Cycles*, *18*(4). doi: 10.1029/2004GB002220

Moore, J. K., Doney, S. C., Lindsay, K., Mahowald, N., & Michaels, A. F. (2006, Jan). Nitrogen fixation amplifies the ocean biogeochemical response to decadal timescale variations in mineral dust deposition. *Tellus B: Chemical and Physical Meteorology*, *58*(5), 560–572. Retrieved from http://dx.doi.org/10.1111/j.1600-0889.2006.00209.x doi: 10.1111/j.1600-0889.2006.00209.x

Moore, J. K., Fu, W., Primeau, F., Britten, G. L., Lindsay, K., Long, M. C., ... Randerson, J. T. (2018). Sustained climate warming drives declining marine biological productivity. *Science*, *359*(6380), 1139-1143. doi: 10.1126/science.aao6379

Moore, J. K., Lindsay, K., Doney, S. C., Long, M. C., & Misumi, K. (2013). Marine ecosystem dynamics and biogeochemical cycling in the Community Earth System Model [CESM1(BGC)]: Comparison of the 1990s with the 2090s under the RCP4.5 and RCP8.5 scenarios. *J. Clim.*, *26*(23), 9291-9312. doi: 10.1175/JCLI-D-12-00566.1

O'Neill, B. C., Tebaldi, C., van Vuuren, D. P., Eyring, V., Friedlingstein, P., Hurtt, G., ... Sanderson, B. M. (2016). The Scenario Model Intercomparison Project (ScenarioMIP) for CMIP6. *Geosci. Model Dev.*, *9*(9), 3461–3482. doi: 10.5194/gmd-9-3461-2016

O'Neill, R., DeAngelis, D., Pastor, J., Jackson, B., & Post, W. (1989, August). Multiple nutrient limitations in ecological models. *Ecological Modelling*, *46*(3-4), 147–163. doi: 10.1016/0304-3800(89)90015-X

Orr, J. C., Najjar, R. G., Aumont, O., Bopp, L., Bullister, J. L., Danabasoglu, G.,

... Yool, A. (2017). Biogeochemical protocols and diagnostics for the CMIP6 Ocean Model Intercomparison Project (OMIP). *Geosci. Model Dev.*, *10*(6), 2169–2199. Retrieved from https://gmd.copernicus.org/articles/10/2169/2017/ doi: 10.5194/gmd-10-2169-2017

Paulot, F., Jacob, D. J., Johnson, M. T., Bell, T. G., Baker, A. R., Keene, W. C., ... Stock, C. A. (2015). Global oceanic emission of ammonia: Constraints from seawater and atmospheric observations. *Global Biogeochem. Cycles*, *29*(8), 1165–1178. doi: 10.1002/2015gb005106

Primeau, F. W., Holzer, M., & DeVries, T. (2013, May). Southern ocean nutrient trapping and the efficiency of the biological pump. *Journal of Geophysical Research, C: Oceans*, *118*(5), 2547–2564. doi: 10.1002/jgrc.20181

Ragueneau, O., Tréguer, P., Leynaert, A., Anderson, R., Brzezinski, M., DeMaster, D., ... et al. (2000, Dec). A review of the Si cycle in the modern ocean: recent progress and missing gaps in the application of biogenic opal as a paleoproductivity proxy. *Global and Planetary Change*, *26*(4), 317–365. Retrieved from http://dx.doi.org/10.1016/S0921-8181(00)00052-7 doi: 10.1016/s0921-8181(00)00052-7

Randerson, J. T., Lindsay, K., Munoz, E., Fu, W., Moore, J. K., Hoffman, F. M., ... Doney, S. C. (2015). Multicentury changes in ocean and land contributions to the climate-carbon feedback. *Global Biogeochem. Cycles*, *29*, 744-759. doi: 10.1002/2014GB005079

Resplandy, L., Keeling, R. F., Rödenbeck, C., Stephens, B. B., Khatiwala, S., Rodgers, K. B., ... Tans, P. P. (2018, June). Revision of global carbon fluxes based on a reassessment of oceanic and riverine carbon transport. *Nature geoscience*, *11*(7), 504–509. doi: 10.1038/s41561-018-0151-3

Ringler, T., Petersen, M., Higdon, R. L., Jacobsen, D., Jones, P. W., & Maltrud, M. (2013, Sep). A multi-resolution approach to global ocean modeling. *Ocean Modelling*, *69*, 211–232. Retrieved from http://dx.doi.org/10.1016/j.ocemod.2013.04.010 doi: 10.1016/j.ocemod.2013.04.010

Rothenberg, D., Mahowald, N., Lindsay, K., Doney, S. C., Moore, J. K., & Thornton, P. (2012). Volcano impacts on climate and biogeochemistry in a coupled carbon–climate model. *Earth System Dynamics*, *3*(2), 121–136. doi: 10.5194/esd-3-121-2012

Sabine, C. L., Feely, R. A., Gruber, N., Key, R. M., Lee, K., Bullister, J. L., ... Rios, A. F. (2004). The oceanic sink for anthropogenic CO_2. *Science*, *305*(5682), 367–371. doi: 10.1126/science.1097403

Sañudo-Wilhelmy, S. A., Kustka, A. B., Gobler, C. J., Hutchins, D. A., Yang, M., Lwiza, K., ... Carpenter, E. J. (2001). Phosphorus limitation of nitrogen fixation by Trichodesmium in the central Atlantic Ocean. *Nature*, *411*(6833), 66–69. Retrieved from https://doi.org/10.1038/35075041 doi: 10.1038/35075041

Sarmiento, J., & Gruber, N. (2006). *Ocean Biogeochemical Dynamics*. Princeton University Press.

Sarmiento, J. L., Gruber, N., Brzezinski, M. A., & Dunne, J. (2004). High-latitude controls of thermocline nutrients and low latitude biological productivity. *Nature*, *427*(6969), nature02127. doi: 10.1038/nature02127

Sarmiento, J. L., Simeon, J., Gnanadesikan, A., Gruber, N., Key, R. M., & Schlitzer, R. (2007, March). Deep ocean biogeochemistry of silicic acid and nitrate. *Global Biogeochem. Cycles*, *21*(1). doi: 10.1029/2006gb002720

Schlitzer, R., Anderson, R. F., Dodas, E. M., Lohan, M., Geibert, W., Tagliabue, A., ... Zurbrick, C. (2018, August). The GEOTRACES intermediate data product 2017. *Chemical geology*, *493*, 210–223. doi: 10.1016/j.chemgeo.2018.05.040

Schwinger, J., Tjiputra, J. F., Heinze, C., Bopp, L., Christian, J. R., Gehlen, M., ... Totterdell, I. (2014, June). Nonlinearity of ocean carbon cycle feedbacks in CMIP5 earth system models. *Journal of climate*, *27*(11), 3869–3888. doi: 10.1175/JCLI-D-13-00452.1

Séférian, R., Berthet, S., Yool, A., Palmiéri, J., Bopp, L., Tagliabue, A., ... Yamamoto, A. (2020, aug). Tracking improvement in simulated marine biogeochemistry between CMIP5 and CMIP6. *Current Climate Change Reports*, *6*(3), 95–119. Retrieved from https://doi.org/10.1007%2Fs40641-020-00160-0 doi: 10.1007/s40641-020-00160-0

Shchepetkin, A. F., & McWilliams, J. C. (2005, January). The regional oceanic modeling system (ROMS): a split-explicit, free-surface, topography-following-coordinate oceanic model. *Ocean Modelling*, *9*(4), 347–404. doi: 10.1016/j.ocemod.2004.08.002

Sherman, E., Moore, J. K., Primeau, F., & Tanouye, D. (2016, April). Temperature influence on phytoplankton community growth rates. *Global biogeochemical cycles*, *30*(4), 550–559. doi: 10.1002/2015gb005272

Siegel, D. A., Buesseler, K. O., Doney, S. C., Sailley, S. F., Behrenfeld, M. J., & Boyd, P. W. (2014, March). Global assessment of ocean carbon export by combining satellite observations and food-web models. *Global Biogeochem. Cycles*, *28*(3), 181–196. doi: 10.1002/2013gb004743

Small, R. J., DuVivier, A. K., Whitt, D. B., Long, M. C., Grooms, I., & Large, W. G. (2020, October). On the control of subantarctic stratification by the ocean circulation. *Climate Dynamics*. doi: 10.1007/s00382-020-05473-2

Stock, C. A., Alexander, M. A., Bond, N. A., Brander, K. M., Cheung, W. W. L., Curchitser, E. N., ... Haltuch, M. A. (2011). On the use of IPCC-class models to assess the impact of climate on living marine resources. *Progress in Oceanography*, *88*(1), 1–27. doi: 10.1016/j.pocean.2010.09.001

Straile, D. (1997). Gross growth efficiencies of protozoan and metazoan zooplankton and their dependence on food concentration, predator-prey weight ratio, and taxonomic group. *Limnology and Oceanography*, *42*(6), 1375-1385. doi: https://doi.org/10.4319/lo.1997.42.6.1375

Sun, Q., Whitney, M. M., Bryan, F. O., & Tseng, Y.-H. (2017, April). A box model for representing estuarine physical processes in earth system models. *Ocean Modelling*, *112*, 139–153. doi: 10.1016/j.ocemod.2017.03.004

Sweeney, C., Gloor, E., Jacobson, A. R., Key, R. M., McKinley, G., Sarmiento, J. L., & Wanninkhof, R. (2007, June). Constraining global air-sea gas exchange for CO_2 with recent bomb ^{14}C measurements. *Global biogeochemical cycles*, *21*(2). doi: 10.1029/2006gb002784

Tagliabue, A., Aumont, O., DeAth, R., Dunne, J. P., Dutkiewicz, S., Galbraith, E., ... Yool, A. (2016). How well do global ocean biogeochemistry models simulate dissolved iron distributions? *Global Biogeochem. Cycles*, *30*(2), 149–174. doi: 10.1002/2015GB005289

Tagliabue, A., Mtshali, T., Aumont, O., Bowie, A. R., Klunder, M. B., Roychoudhury, A. N., & Swart, S. (2012, June). A global compilation of dissolved iron measurements: focus on distributions and processes in the Southern Ocean. *Biogeosciences*, *9*(6), 2333–2349. doi: 10.5194/bg-9-2333-2012

Tagliabue, A., Sallée, J.-B., Bowie, A. R., Lévy, M., Swart, S., & Boyd, P. W. (2014, March). Surface-water iron supplies in the southern ocean sustained by deep winter mixing. *Nature geoscience*, *7*(4), 314–320. doi: 10.1038/ngeo2101

Thornton, P. E., Doney, S. C., Lindsay, K., Moore, J. K., Mahowald, N., Randerson, J. T., ... Lee, Y.-H. (2009). Carbon-nitrogen interactions regulate climate-carbon cycle feedbacks: results from an atmosphere-ocean general circulation model. *Biogeosciences Discussions*, *6*(2), 3303–3354. doi: 10.5194/bgd-6-3303-2009

Tommasi, D., Stock, C. A., Hobday, A. J., Methot, R., Kaplan, I. C., Eveson, J. P., ... et al. (2017). Managing living marine resources in a dynamic environment: The role of seasonal to decadal climate forecasts. *Progress in Oceanography*, *152*, 15–49. doi: 10.1016/j.pocean.2016.12.011

Wang, S., Moore, J. K., Primeau, F. W., & Khatiwala, S. (2012). Simulation of

anthropogenic CO_2 uptake in the CCSM3.1 ocean circulation-biogeochemical model: comparison with data-based estimates. *Biogeosciences*, *9*(4), 1321–1336. doi: 10.5194/bg-9-1321-2012

Wang, W.-L., Moore, J. K., Martiny, A. C., & Primeau, F. W. (2019). Convergent estimates of marine nitrogen fixation. *Nature*, *566*(7743), 205–211. doi: 10.1038/s41586-019-0911-2

Wu, J., Sunda, W., Boyle, E. A., & Karl, D. M. (2000). Phosphate depletion in the western North Atlantic Ocean. *Science*, *289*(5480), 759–762. Retrieved from https://science.sciencemag.org/content/289/5480/759 doi: 10.1126/science.289.5480.759

Yeager, S., Karspeck, A., Danabasoglu, G., Tribbia, J., & Teng, H. (2012, Aug). A decadal prediction case study: Late twentieth-century North Atlantic Ocean heat content. *Journal of Climate*, *25*(15), 5173–5189. doi: 10.1175/jcli-d-11-00595.1

Yeager, S. G., Danabasoglu, G., Rosenbloom, N. A., Strand, W., Bates, S. C., Meehl, G. A., … Lovenduski, N. S. (2018, September). Predicting Near-Term changes in the earth system: A large ensemble of initialized decadal prediction simulations using the Community Earth System Model. *Bulletin of the American Meteorological Society*, *99*(9), 1867–1886. doi: 10.1175/BAMS-D-17-0098.1

Yeager, S. G., Shields, C. A., Large, W. G., & Hack, J. J. (2006). The low-resolution CCSM3. *Journal of Climate*, *19*(11), 2545–2566. doi: 10.1175/jcli3744.1

Zehr, J. P., & Capone, D. G. (2021). N_2 fixation in ocean basins. In *Marine nitrogen fixation* (pp. 143–156). Cham: Springer International Publishing. Retrieved from https://doi.org/10.1007/978-3-030-67746-6_8 doi: 10.1007/978-3-030-67746-6_8

Zweng, M., Reagan, J., Seidov, D., Boyer, T., Locarnini, R., Garcia, H., … Smolyar, I. (2019). *World Ocean Atlas 2018, Volume 2: Salinity* (Vol. NOAA Atlas NESDIS 82). U.S. Department of Commerce. Retrieved from http://www.nodc.noaa.gov/OC5/indprod.html

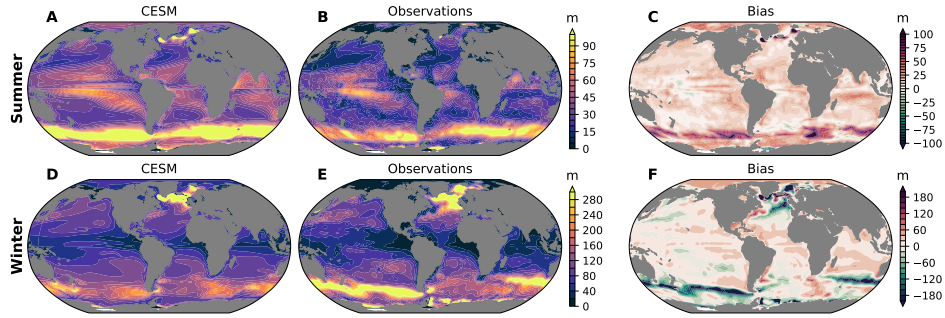

Figure 1. Climatological mixed layer depth (A,D) simulated by CESM2 over 1990–2014 compared with (B,F) observationally-based estimates of mixed layer depth from WOA2013. The right column shows model biases (C,F). Mixed layer depth was computed using a $\Delta_{\sigma_\theta} = 0.125$ criterion (Monterey & Levitus, 1997). The top row shows summertime distributions, which correspond to June–August means in the Northern Hemisphere and December–February means in the Southern Hemisphere (A-C). These seasons are reversed for each hemisphere in the bottom row, which shows winter (D-F).

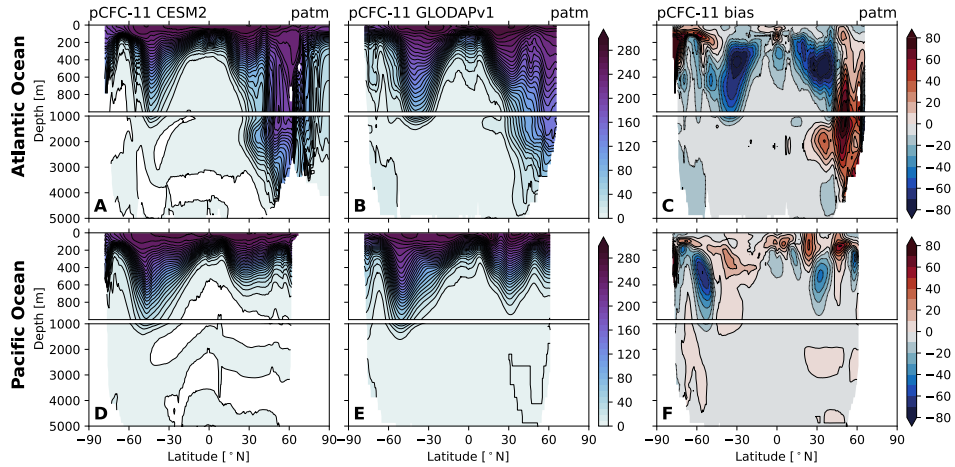

Figure 2. CESM-simulated zonal-mean partial pressure of CFC-11 (pCFC-11) for 1990–2000 (A,D) compared with observations from GLODAPv1 (B,E) (Key et al., 2004). The right column shows model biases (C,F). The top row is the distributions for the Atlantic Ocean (A-C) and the bottom row is the Pacific Ocean distributions (D-F).

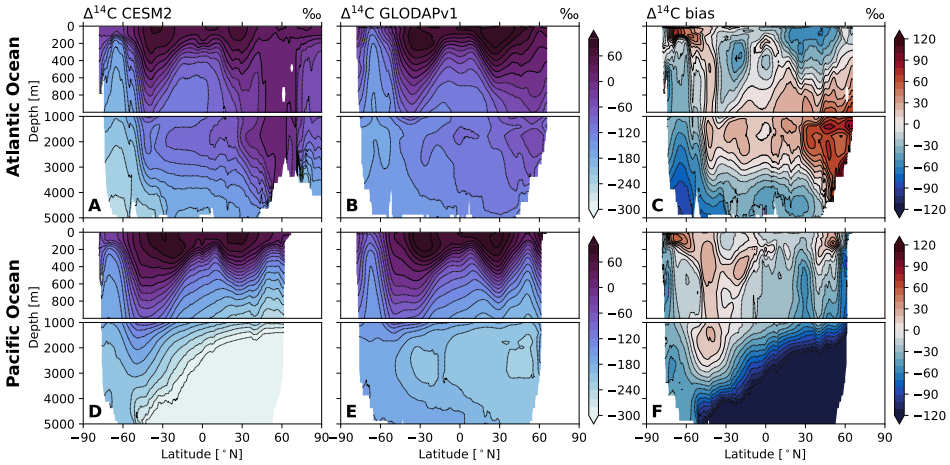

Figure 3. CESM-simulated zonal-mean radiocarbon (^{14}C) distributions for 1990–2000 (A,D) compared with observations from GLODAPv1 (B,E) (Key et al., 2004). The right column shows model biases (C,F). The top row is the distributions for the Atlantic Ocean (A-C) and the bottom row is the Pacific Ocean distributions (D-F).

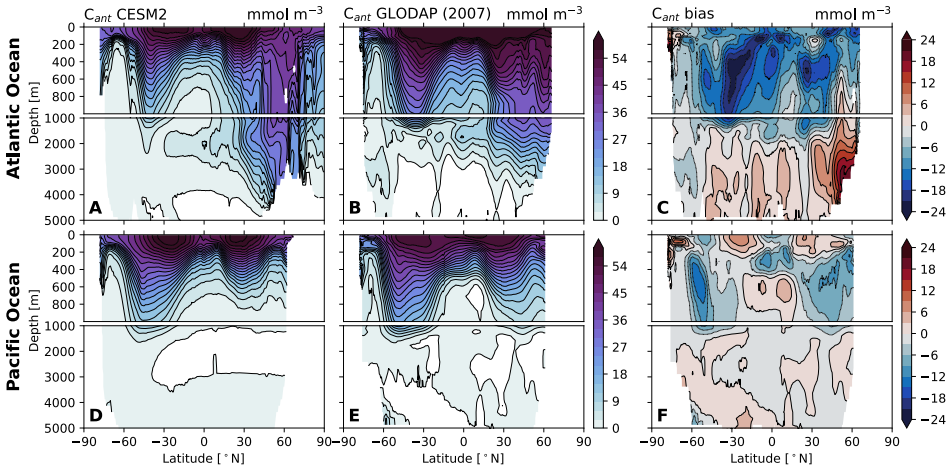

Figure 4. CESM-simulated zonal-mean anthropogenic carbon inventory (C_{ant}) for 2007 (A,D) compared with observations from GLODAPv1 (B, E) (Key et al., 2004) and adjusted for uptake between 1994–2007 (Gruber et al., 2019). The right column shows model biases (C,F). The top row is the distributions for the Atlantic Ocean (A-C) and the bottom row is the Pacific Ocean distributions (D-F).

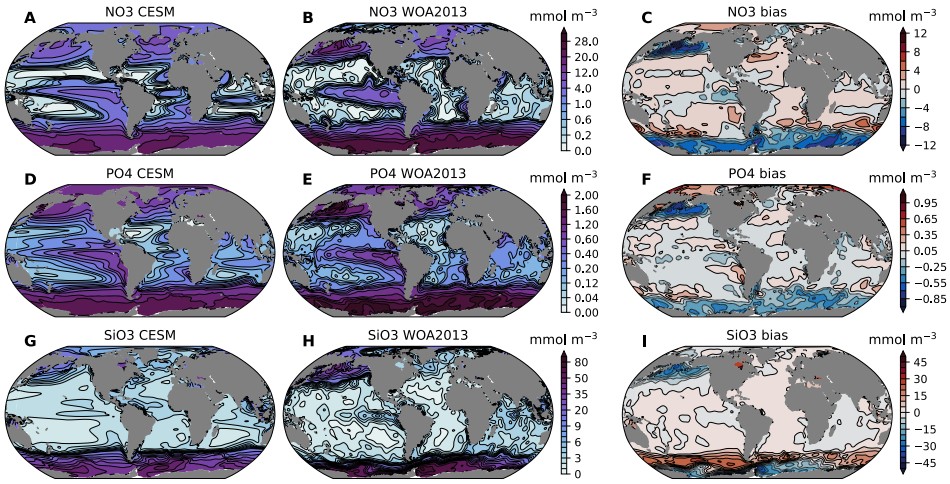

Figure 5. CESM simulated annual mean surface nitrate (A), phosphate (D), and silicate concentrations (G) for 1990–2014 compared with observations from the World Ocean Atlas, 2018 (B,E,H) (Garcia et al., 2018). Note non-linear color scales. The right column shows model biases (C,F,I).

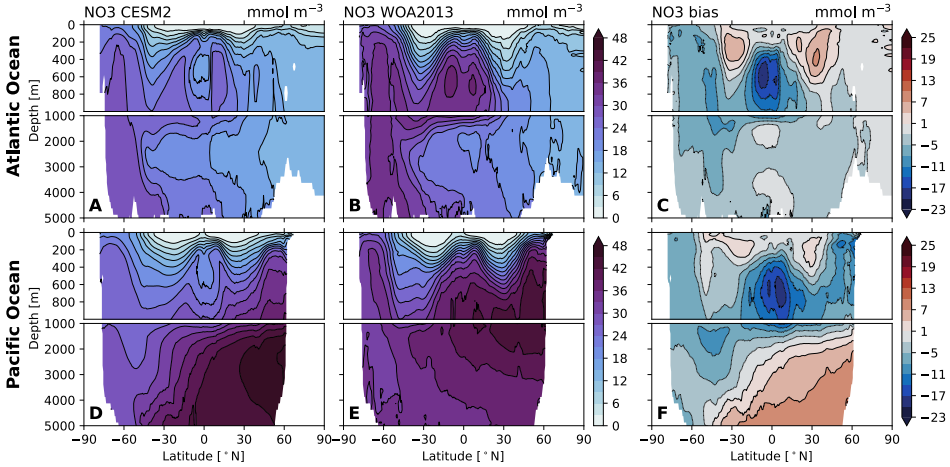

Figure 6. CESM-simulated annual mean of zonal-mean nitrate (NO_3) distributions for 1990–2014 compared with the World Ocean Atlas, 2018 (Garcia et al., 2018) (B,E). The right column shows model biases (C,F). The top row is the distributions for the Atlantic Ocean (A-C) and the bottom row is the Pacific Ocean distributions (D-F).

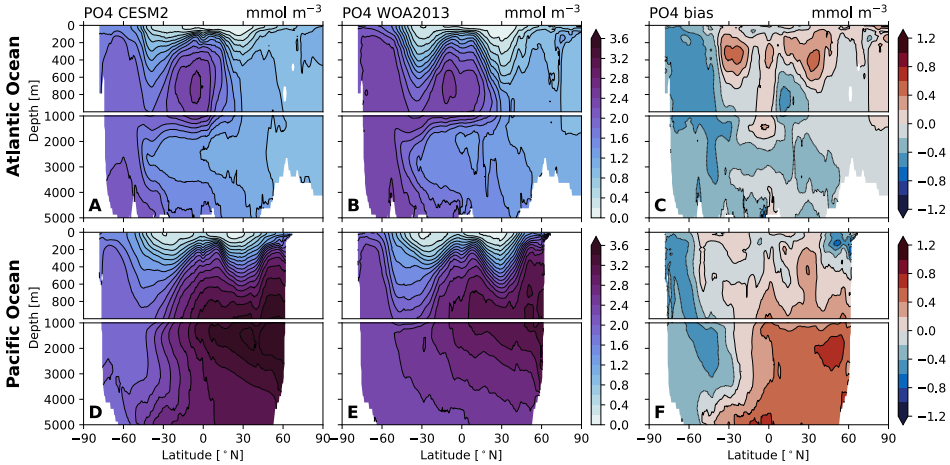

Figure 7. CESM simulated annual mean, zonal-mean phosphate for 1990–2014 compared with World Ocean Atlas, 2018 (Garcia et al., 2018) (B,E). The right column shows model biases (C,F). The top row is the distributions for the Atlantic Ocean (A-C) and the bottom row is the Pacific Ocean distributions (D-F).

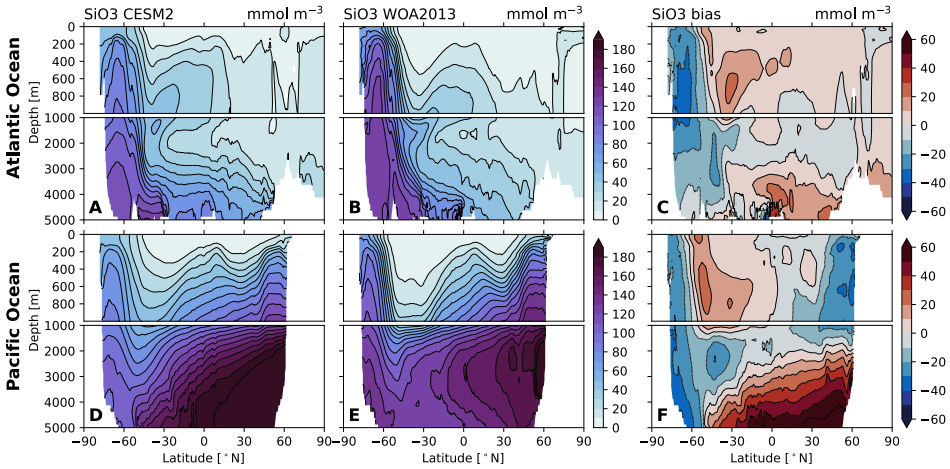

Figure 8. CESM simulated annual mean, zonal-mean silicate for 1990–2014 compared with observations from the World Ocean Atlas, 2018 (Garcia et al., 2018) (B,E). The right column shows model biases (C,F). The top row is the distributions for the Atlantic Ocean (A-C) and the bottom row is the Pacific Ocean distributions (D-F).

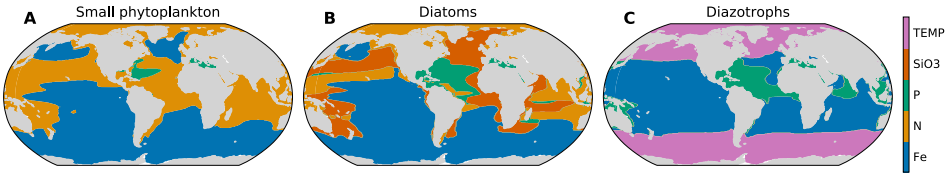

Figure 9. The factor most limiting phytoplankton growth for annual means over the period 1990–2014. Limitation terms (with the exception of temperature) are computed as biomass-weighted vertical averages. The temperature term for diazotrophs is approximated by applying the temperature threshold for growth (15°C) to annual-mean sea surface temperature.

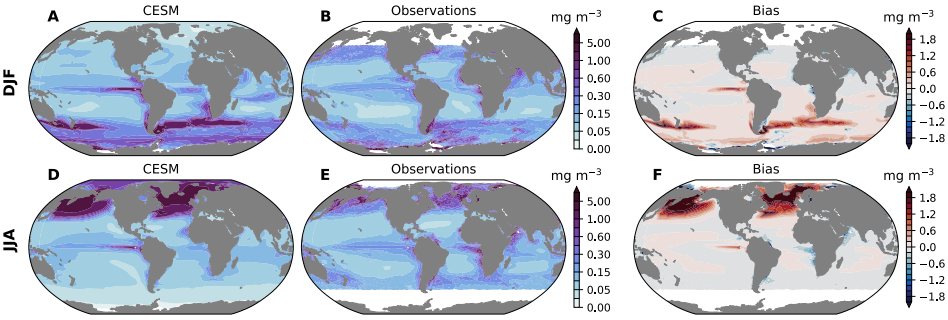

Figure 10. A comparison of SeaWiFS satellite derived chlorophyll concentration to CESM-simulated surface chlorophyll (top 10 m). The top row shows December-January-February (DJF) means, while the bottom row shows June-July-August (JJA) means. SeaWiFS observations are a mean over the period 1997 to 2010, while model means computed over the period 1990 to 2014.

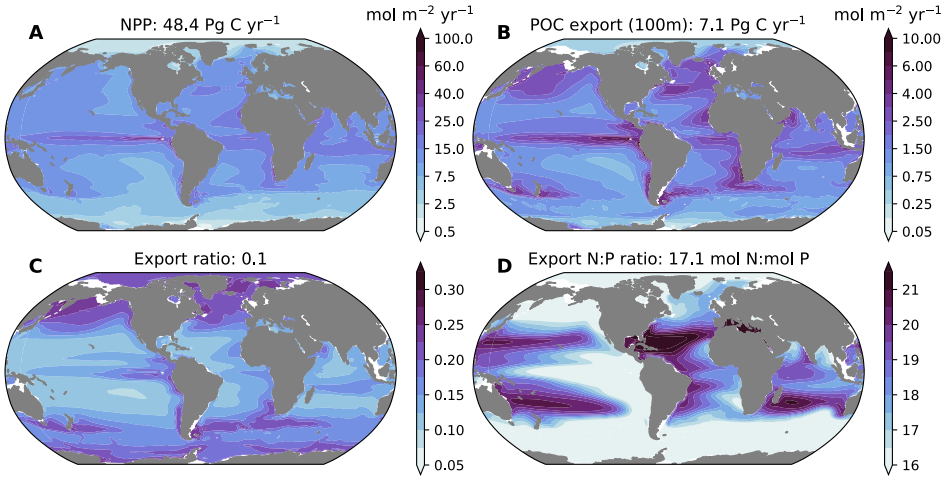

Figure 11. Net primary production (NPP) and organic matter export in CESM2 over the period 1990–2014. (A) NPP and (B) particulate organic matter (POC) export at 100 m in mol m^{-2} yr^{-1}, with globally integrated values indicated in the title of each panel. (C) The export ratio (i.e., pe-ratio = sinking export/NPP) and (D) the N:P ratio of exported biomass, with global mean values indicated in title of each panel.

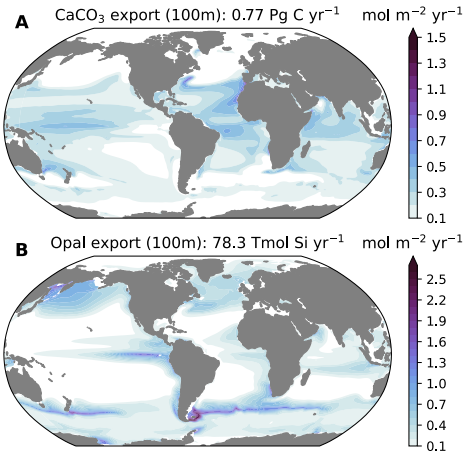

Figure 12. Mineral fluxes in CESM2 over the period 1990–2014. (A) $CaCO_3$ export at 100 m; (B) opal export at 100 m. Globally-integrated fluxes are indicated in the title above each panel.

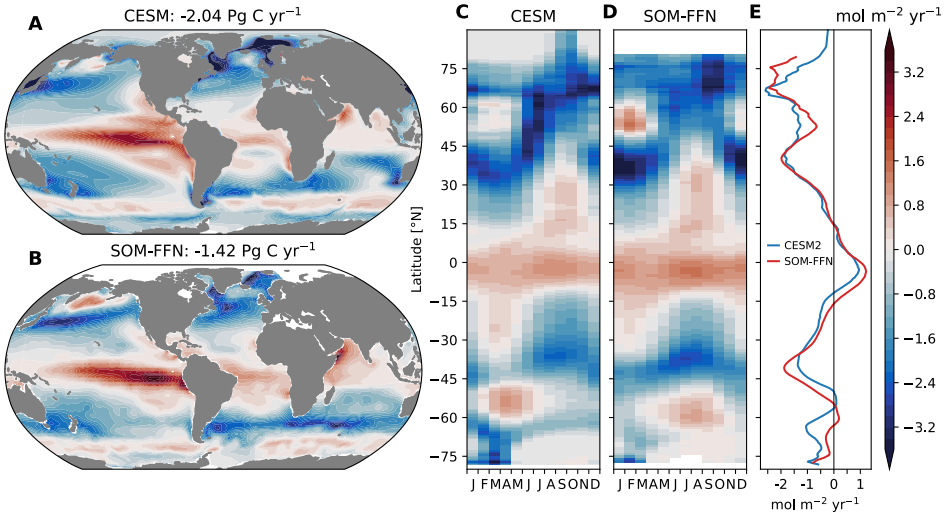

Figure 13. Air-sea CO_2 flux. (A) Simulated annual-mean air-sea CO_2 flux from CESM2 over the period 1990–2014. (B) Observationally-based estimate of air-sea CO_2 (Landschützer et al., 2017) based on the method of Landschützer et al. (2016).

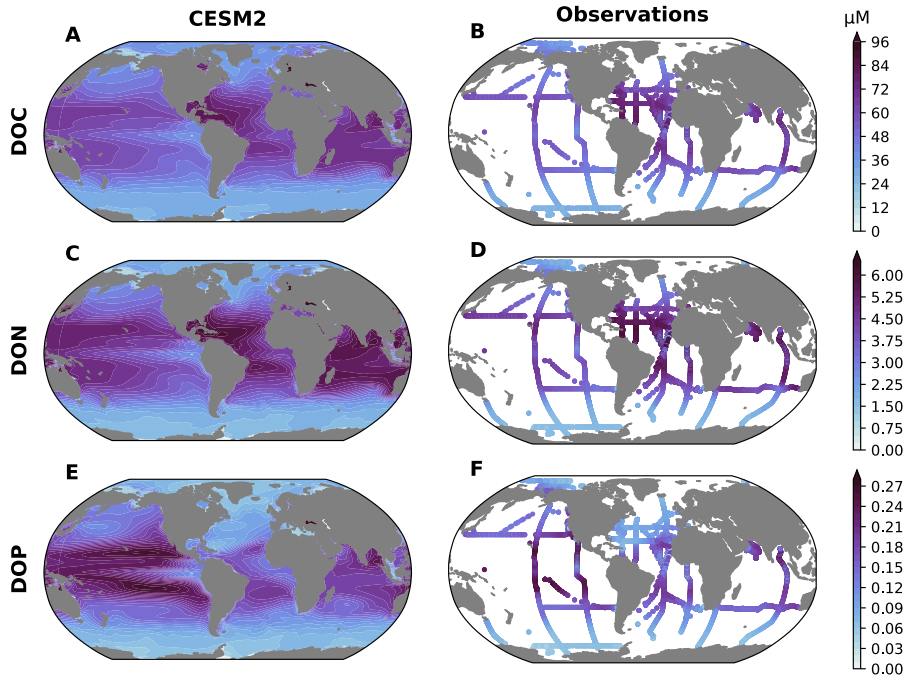

Figure 14. Simulated (left) and observed (right) concentrations of dissolved organic matter (μM) in the upper 100 m. (A, B) dissolved organic carbon; (C, D) dissolved organic nitrogen; (E, F) dissolved organic phosphorus. The observations are from Letscher and Moore (2015).

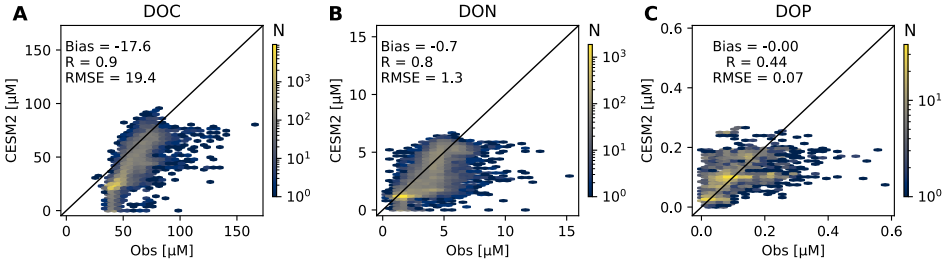

Figure 15. Comparison of simulated dissolved organic matter concentrations with observations over the upper 1000 m of the water column. Two-dimensional histograms of simulated versus observed concentrations (μM) for (A) dissolved organic carbon; (B) dissolved organic nitrogen; (C) dissolved organic phosphorus. Colors show the number of model-observation pairs in each bin; the black diagonal line shows a 1:1 relationship; inset text indicates mean bias, correlation, and root mean squared error (RMSE). The observations are from Letscher and Moore (2015).

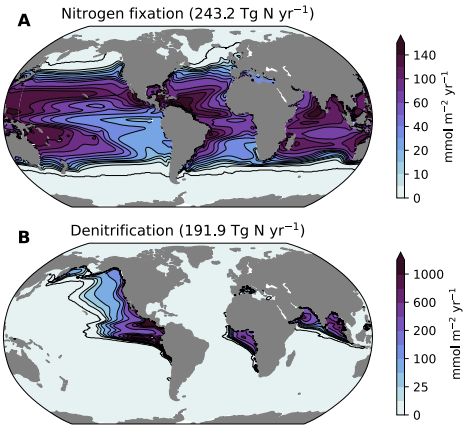

Figure 16. Annual mean (A) nitrogen fixation and (B) water column denitrification simulated by CESM2 for the period 1990–2014. Global integrals are reported in the figure titles.

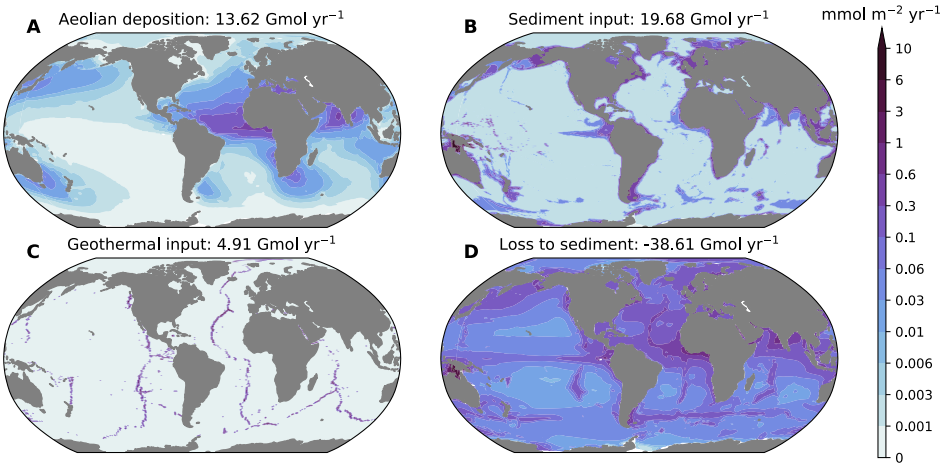

Figure 17. Spatial distribution of dominant terms in the CESM2 global iron budget. (A) Atmospheric deposition; (B) total sedimentary input, include oxic and reducing sedimentary sources; (C) geothermal input; (D) losses to sediments via burial. The title string of each panel reports the global integral. Note that the atmospheric deposition term includes a subsurface contribution from iron released when sinking dust is remineralized. This contribution accounts for 5.5 Gmol yr^{-1}. Riverine inputs are not shown; these account for 0.37 Gmol yr^{-1}.

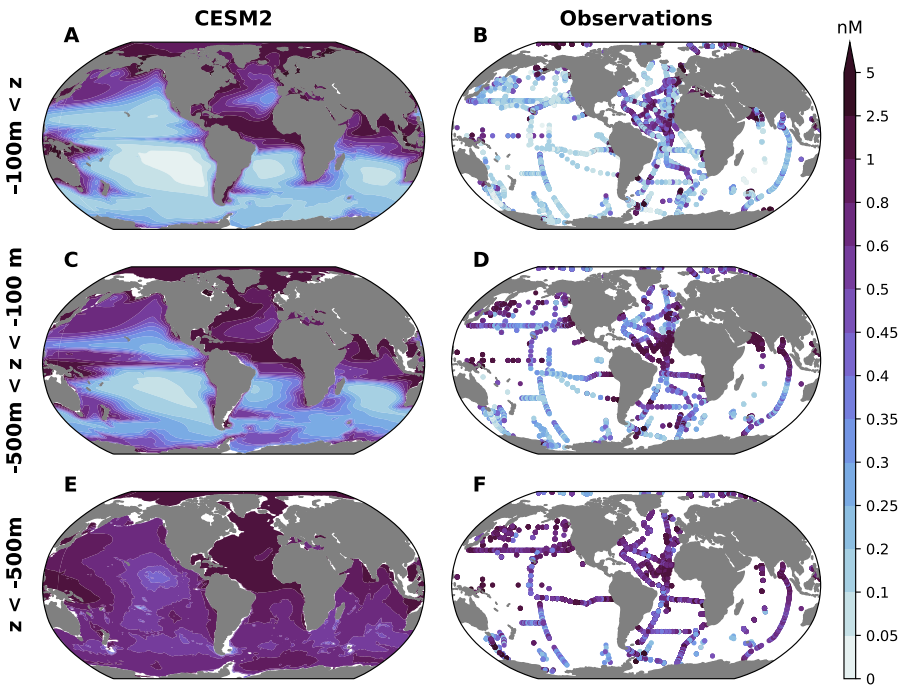

Figure 18. Dissolved iron concentrations in (left panels) CESM2 simulations over 1990–2014 and (right panels) observations from Schlitzer et al. (2018) with additional observations compiled by Tagliabue et al. (2012) and Moore and Braucher (2008). The rows show different depth ranges: (A, B) above 100 m, (C, D) between 500 m and 100 m and (E, F) below 500 m.

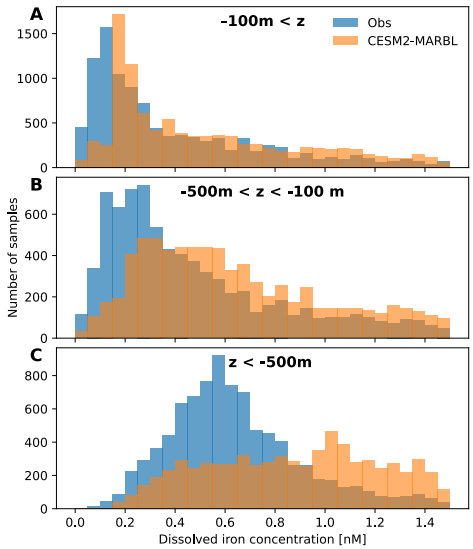

Figure 19. Histograms of dissolved iron concentrations in CESM2 simulations over 1990–2014 and observations. The model results have been sampled at the locations of the observations. The rows show different depth ranges: (A) above 100 m, (B) between 500 m and 100 m and (C) below 500 m.

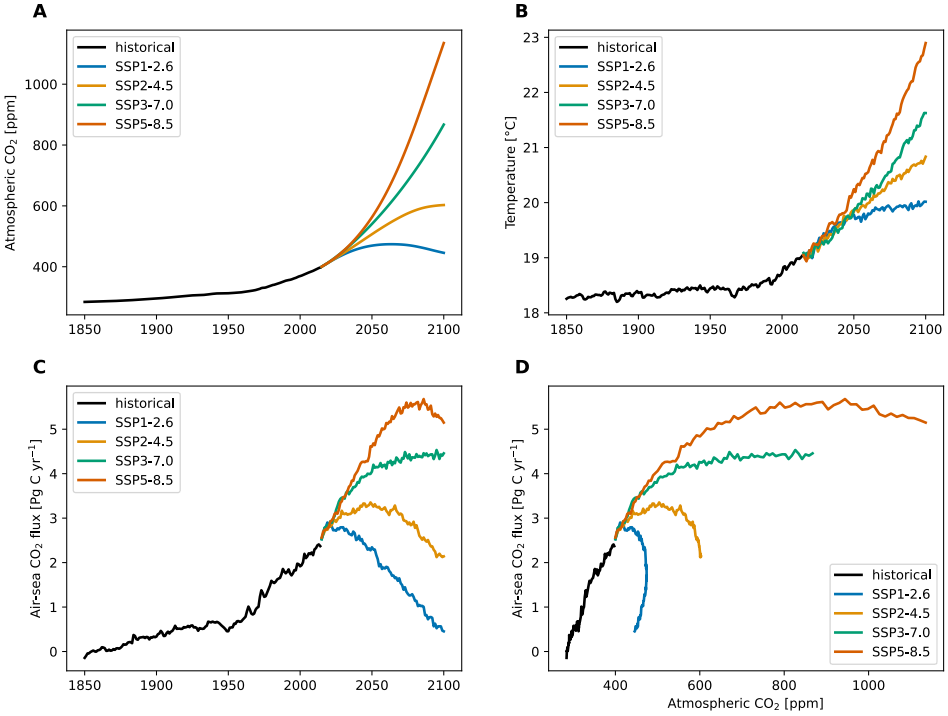

Figure 20. Time series of ensemble-mean (A) prescribed atmospheric CO_2, (B) CESM2 simulated global mean sea surface temperature, (C) globally-integrated air-sea flux. (D) Globally-integrated air-sea CO_2 flux as a function of atmospheric CO_2.

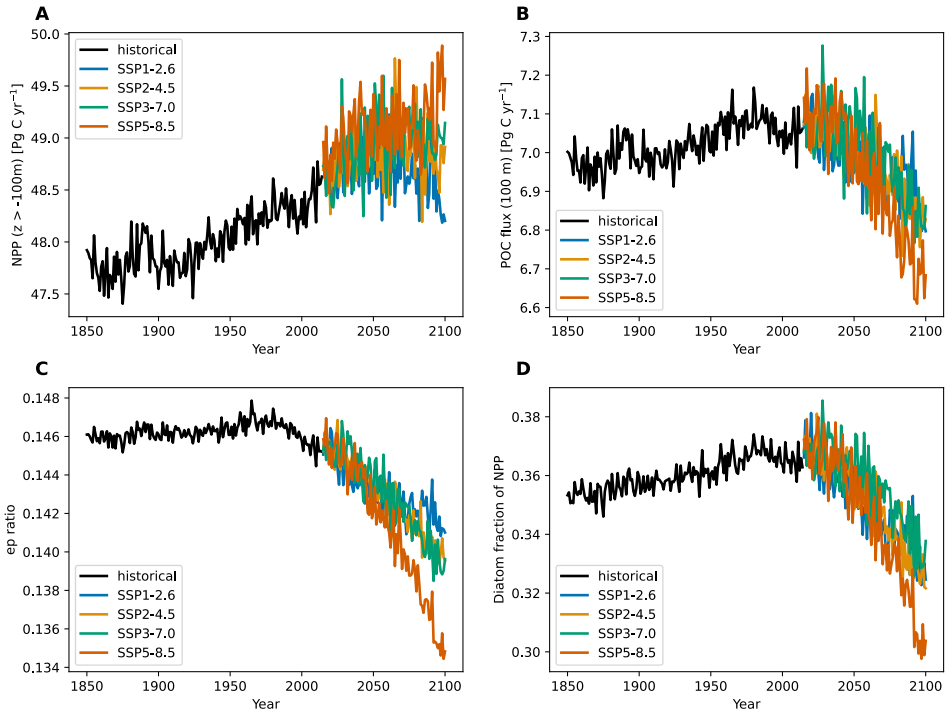

Figure 21. Globally-integrated time series of simulated (A) net primary productivity (B) particulate organic carbon (POC) export at 100 m, (C) particulate export ratio (export/NPP), and (D) the fraction of NPP accomplished by diatoms.

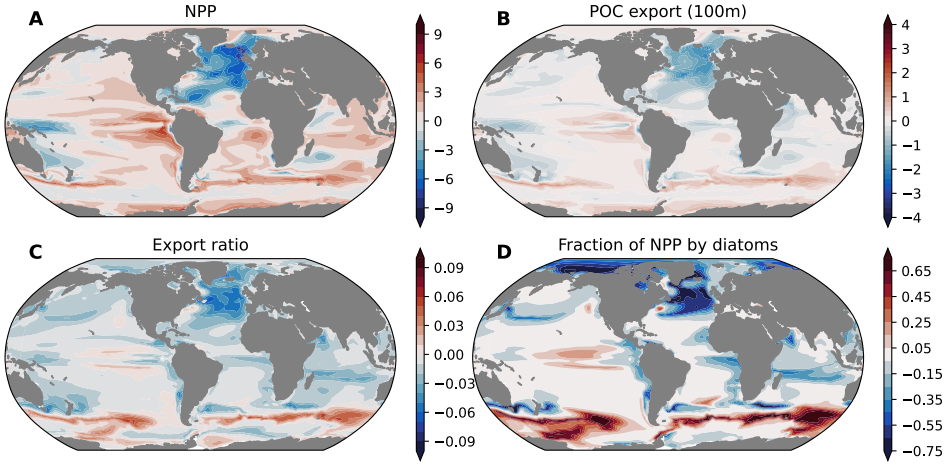

Figure 22. Change between the historical (1990–2014) and end of 21st century (2086–2100) under SSP5-8.5 for (A) net primary productivity (B) particulate organic carbon (POC) export at 100 m, (C) particulate export ratio (sinking export/NPP), and (D) the fraction of NPP accomplished by diatoms.